Modelling patient-specific range of elbow flexion and extension from single computed tomography images

TM30004: Master thesis

Marijke (M.M.J.) ten Elzen

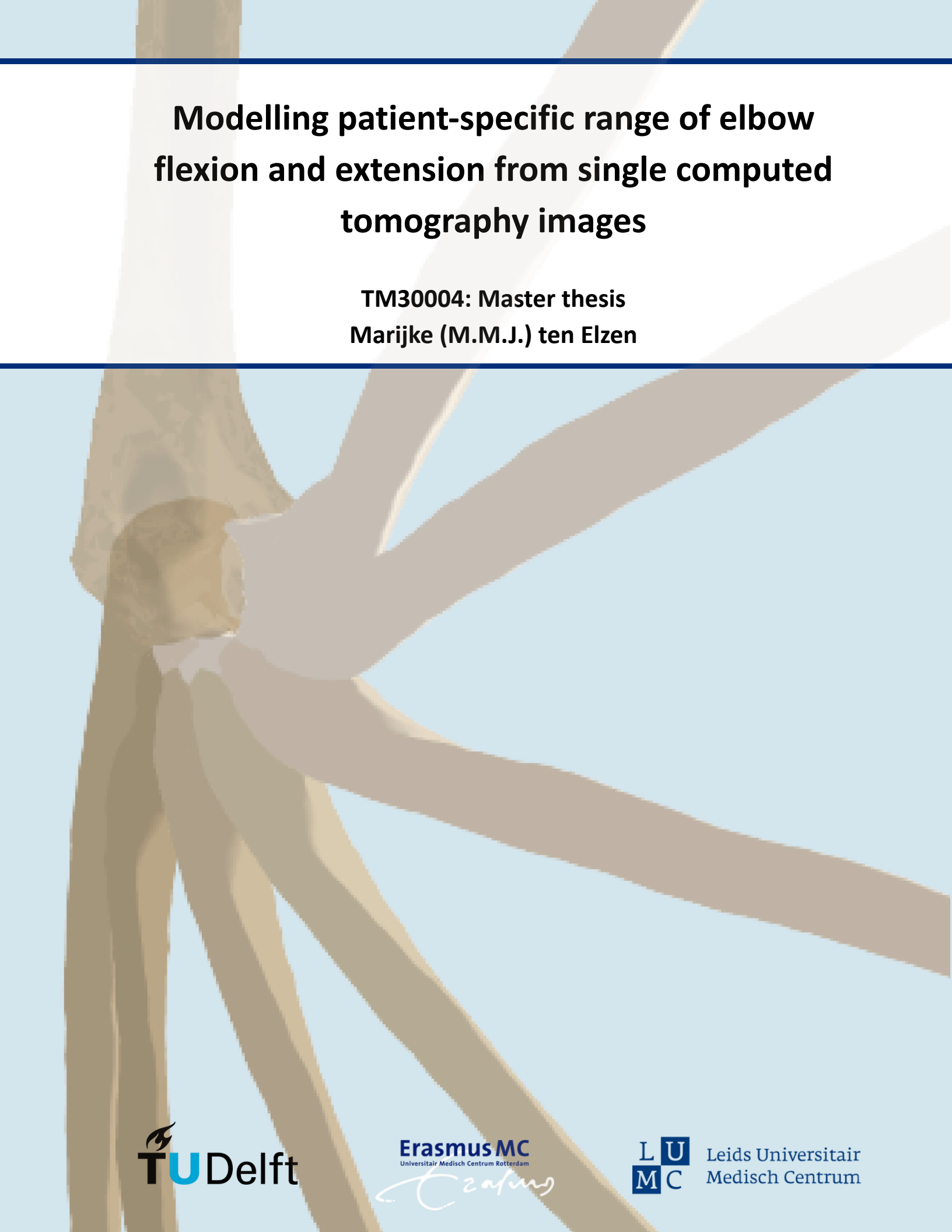

TU Delft

Erasmus MC
Universitair Medisch Centrum Rotterdam

LUMC Leids Universitair Medisch Centrum

MODELLING PATIENT-SPECIFIC RANGE OF ELBOW FLEXION AND EXTENSION FROM SINGLE COMPUTED TOMOGRAPHY IMAGES

Marijke ten Elzen

Student number: 4792521

May 26, 2025

Thesis in partial fulfilment of the requirements for the joint degree of Master of Science in

Technical Medicine

Leiden University - Delft University of Technology - Erasmus University Rotterdam

Master thesis project (TM30004 - 35 ECTS)
Dept. of Orthopedics & Sports Medicine, Erasmus MC
November 2024 – May 2025

Supervisor(s):
Prof. Dr. H.E.J. Veeger
Dr. J.W. Colaris
E.M. van Es, MSc
D.F.R. van Loon, MSc
M.F. Siemensma, MD

Thesis committee members:
Prof. Dr. H.E.J. Veeger – TU Delft (chair)
Dr. J.W. Colaris – Erasmus MC
Dr. E.A. van der Windt – Erasmus MC
E.M. van Es, MSc – Erasmus MC

Table of Contents

Summary

Introduction: Unrestricted elbow range of motion (ROM) is essential for daily function, yet flexion and extension limitations frequently occur following elbow trauma. These restrictions may result from osseous deformities, soft tissue contracture, or both, requiring accurate identification of the dominant cause to guide treatment. Although CT imaging provides detailed evaluations of bony pathology, conventional single CT lacks functional information, and dynamic 4D-CT faces clinical limitations. Therefore, alternative approaches to assess osseous contributions to motion restrictions are needed.

Objective: This study aims to introduce and validate a 3D computational kinematic bone model based on segmented single CT scans. The model enables patient-specific simulation of elbow flexion and extension, enabling quantifiable assessment of osseous related motion restrictions to support clinical decision making.

Methods: Eight non-affected cadaveric elbows were scanned using computed tomography in seven positions ranging from full extension to full flexion and segmented into 3D models. Anatomical landmarks were automatically identified to define a landmark-based rotation axis (LMA), which was validated against a kinematically derived average helical axis (AHA). The primary outcomes were the angular deviation and the minimal distance between the axes. The simulated ulnar motion was generated by applying finite helical axis-derived rotations to the neutral ulnar pose. Predicted poses were compared to scanned poses at each flexion angle, with translational and rotational deviations calculated to assess simulation accuracy. Clinical applicability was evaluated by applying the model to bilateral CT scans of ten patients with elbow flexion and extension restrictions. Model-based ROM was determined by simulating flexion and extension and identifying the onset of osseous impingement, and compared to clinically recorded ROM.

Results: Alignment between the LMA and the AHA showed a mean positional difference of 0.41 mm (SD 0.22) and an angular deviation of 2.76° (SD: 1.32). LMA-based simulated ulnar poses demonstrated increasing translational and rotational errors with flexion, predominantly in distal, lateral and valgus directions. Specimens exhibited impingement exclusively in the ulnohumeral region at the trochlea and the greater sigmoid notch. In patients, model-based ROM showed a mean absolute difference of 6.7° for terminal extension and 14.2° for terminal flexion, with false-positive impingement primarily observed in the ulnohumeral region.

Conclusion: This study validated a 3D computational model for simulating elbow flexion and extension using single CT scans. The model accurately estimated ROM and identified osseous impingement locations. Although it demonstrated sensitivity to false-positive detections, it provides a clinically applicable tool for assessing osseous motion restrictions. Future improvement should focus on enhancing landmark accuracy and potentially restricting impingement detection to anatomically relevant regions.

1| Introduction

Unrestricted elbow flexion and extension are essential for positioning the hand in space, facilitating the performance of daily activities. Functional tasks typically require an elbow range of motion (ROM) of 30° to 130° of flexion [1]. However, recent studies suggest that the demand of modern daily activities often exceeds this range, necessitating a greater flexion arc [2]. Consequently, even minor reductions in elbow ROM can severely impair a patient's ability to perform everyday activities, depending on the specific demands of their daily tasks [3]. Such restrictions are common complications following elbow joint trauma [4].

Reduced elbow ROM can either result from intra- and extra-articular changes in osseous anatomy, soft tissue contracture, or a combination of these factors [5]. Osseous constraints arise from osteophyte formation, osteoarthritis, malunions, heterotopic ossification (HO), or loose bodies. Such conditions may disrupt joint congruency and induce pathological bone-on-bone contact during flexion and extension. Soft tissue-related restrictions include adhesions, capsular or ligamentous contractures, and skin contractures following burns, further limiting joint mobility. The impairment is often multifactorial, with both osseous and soft tissue components contributing to the restriction. [6]

Identifying the dominant source of the motion limitation is important, as treatment strategies differ fundamentally. Soft tissue restrictions generally respond well to nonsurgical treatment with physiotherapy and static-progressive bracing. Conversely, osseous restrictions typically require early surgical intervention, such as open or arthroscopic arthrolysis with removal of the osseous constraints. [6] Hence, a thorough diagnostic workup involving physical examination and targeted imaging is needed. Plain radiographs (anteroposterior and lateral views), computed tomography (CT), and magnetic resonance imaging (MRI) enable assessment of joint congruency, degenerative changes, and the presence of osteophytes, HO, or loose bodies, potentially restricting motion. Among these, CT offers the most detailed visualisation of osseous anatomy and is the preferred imaging method when surgical intervention for suspected osseous abnormalities is considered [6].

Although conventional single CT is the standard imaging modality for evaluating osseous pathology, it captures anatomy in a fixed position. It does not provide direct information on how the specific osseous pathology affects the ROM. To address this limitation, dynamic four-dimensional CT (4D-CT) has been explored to enable motion-based analysis of joint function. However, its clinical applicability remains limited due to high radiation exposure, motion artefacts, and complex acquisition protocols, including longer scan and processing times than conventional single CT. As a result, 4D-CT has not been widely adopted in routine clinical practice despite its potential to enhance functional assessment. [7, 8]

3D computational kinematic bone modelling provides a promising alternative, as it overcomes the limitations of 4D-CT. This approach significantly reduces radiation exposure, complexity, and costs by employing standard and readily available static CT data. Our study aims to introduce and validate a computational model that simulates elbow flexion and extension using 3D bone surface models derived from segmented (bilateral) single CT scans. To achieve this, two primary objectives are defined: (1) to determine the validity of an automatically placed landmark-defined axis (LMA) as the rotation axis for elbow flexion and extension by comparing it with a kinematically derived axis, specifically the average

helical axis (AHA); and (2) to assess the model's capability to accurately estimate the ROM in flexion and extension using the LMA as the axis of rotation. ROM is the maximum arc of motion before osseous impingement, characterised by direct contact between bony structures that physically limit motion. By enabling patient-specific and quantifiable analysis of the extent to which individual bony anatomy contributes to ROM restrictions, this model has the potential to improve clinical decision-making and optimise treatment strategies for patients with restricted elbow motion.

2 | Methods

2.1 Evaluation of kinematic rotation axis

2.1.1 Image acquisition and processing

CT scans were acquired from the upper extremity of eight specimens without known trauma or ROM restrictions (age range 61-90 years; seven female). Each specimen was scanned in seven distinct elbow poses with the forearm in a neutral position (thumb pointing upwards). Joint poses were determined using a goniometer, measuring the angle between the long axis of the upper arm and the forearm. Scans were acquired at 30° increments (0°, 30°, 60°, 90°, 120°), in addition to maximum extension and maximum flexion. A custom-made fixation setup was used to ensure consistent positioning across scans (Appendix A). Scans were performed using a Siemens NAEOTOM Alpha CT scanner (Siemens Healthineers AG, Erlangen, Germany).

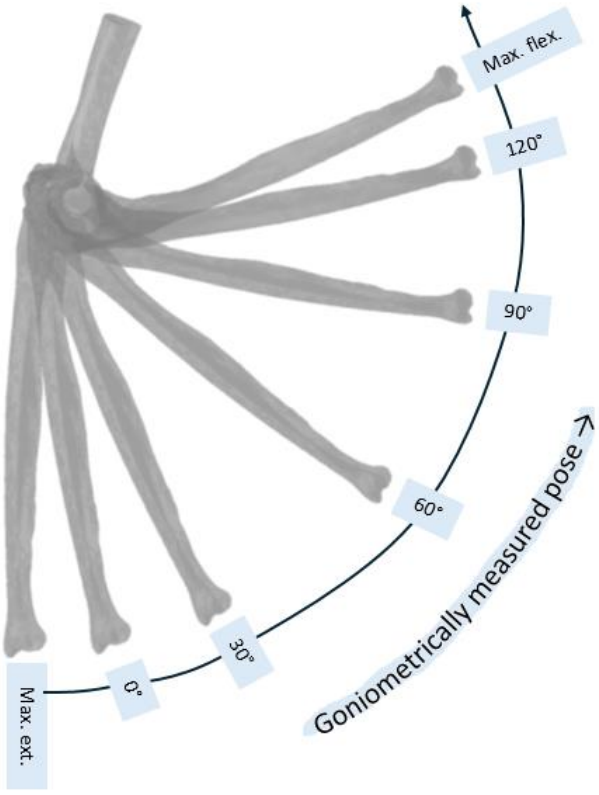

Figure 1:*Schematic representation of the scanned elbow poses used for 3D computational modelling.*

CT data were stored in Digital Imaging and Communications in Medicine (DICOM) format. The humeri and ulnae were segmented using Materialise Mimics Version 26.0 (Materialise NV, Leuven, Belgium). A threshold range of 226 to 3071 Hounsfield units was applied, followed by region-growing techniques and manual refinement. The resulting 3D bone surface models were exported in Standard Tessellation Language (STL) format and imported into 3-Matic (Materialise NV, Leuven, Belgium) for further processing.

Using surface-based alignment, a duplicate of the goniometrically defined 0° model was registered to the corresponding scan for each flexion pose. This approach ensured consistent bone

geometry across all flexion poses. This procedure was performed separately for each specimen. Subsequently, the humerus of the flexed pose was aligned to the goniometrically defined 0° humerus, applying the identical transformation to the corresponding ulna. Fig. 1 illustrates the resulting spatial alignment.

Using the methodologies of Negrillo-Cardenas et al. [9] and van Loon et al. [10], anatomical landmarks were automatically placed on the 3D bone surface models of the humerus and ulna.

2.1.2 Local coordinate systems

Local coordinate systems were defined using the automatically placed anatomical landmarks, primarily following the International Society of Biomechanics (ISB) guidelines [11], with specific adaptations made to match the objectives of this study.

For the humerus (Fig. 2), the origin was placed at the midpoint between the capitellum's and trochlea's centres. The y-axis was aligned with the humeral shaft, directed proximally. The temporary x-axis, pointing anteriorly, was defined as the vector perpendicular to the plane formed by the y-axis and the line connecting the capitellum and trochlea. The z-axis was computed as the cross product of the y- and temporary x-axes, pointing laterally. The final x-axis was recalculated as the cross product of the y- and z-axes to ensure orthogonality.

The ulnar coordinate system (Fig. 3) was defined with the origin at the tip of the coronoid process. The y-axis was defined as the line from the ulnar styloid to the humeral origin, pointing

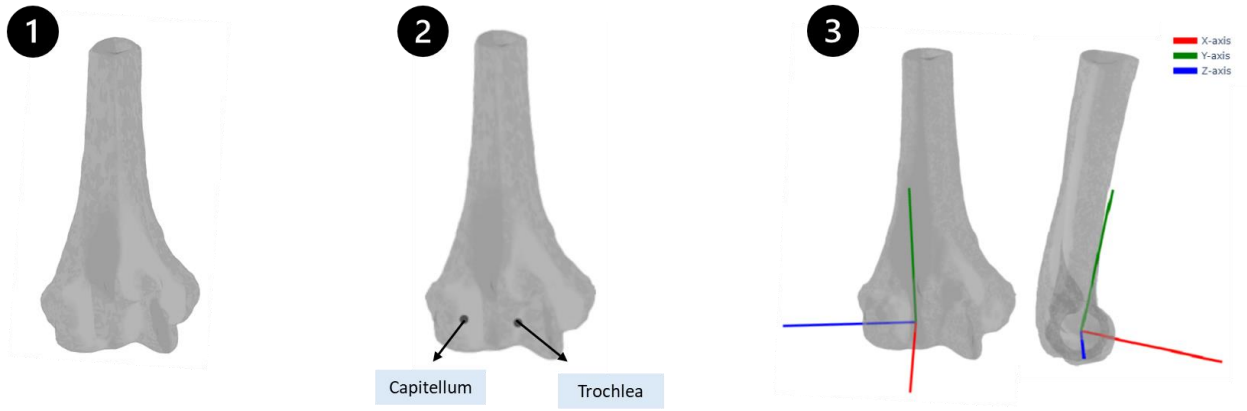

Figure 2: *Local coordinate system of the humerus.*

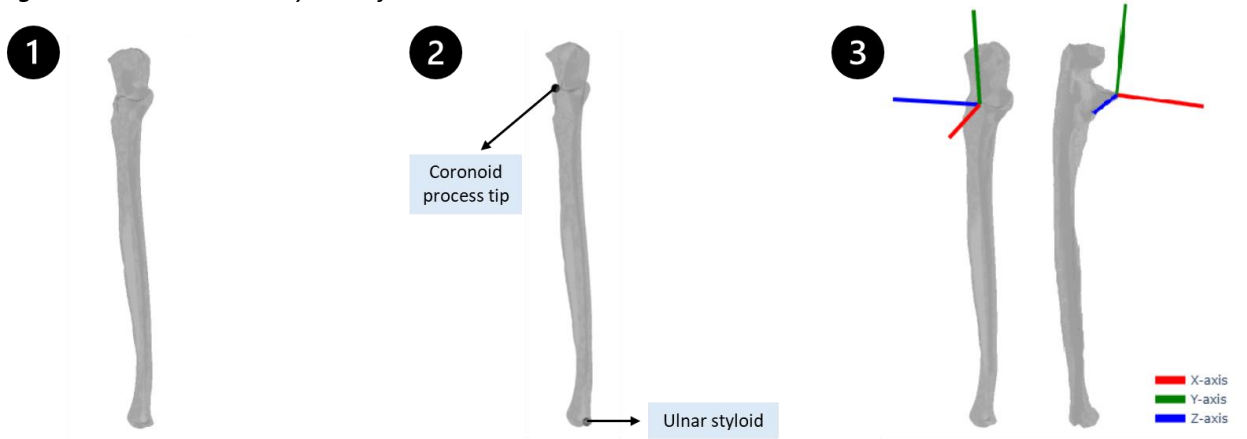

Figure 3: *Local coordinate system of the ulna.*

proximally. A temporary x-axis, directed anteriorly, was computed as the line perpendicular to the plane formed by the ulnar styloid, trochlea, and capitellum. The z-axis, pointing laterally, was computed as the cross product of the y- and temporary x-axes, followed by a recalculation of the x-axis to form an orthogonal system.

2.1.3 Landmark defined versus kinematically derived rotation axis

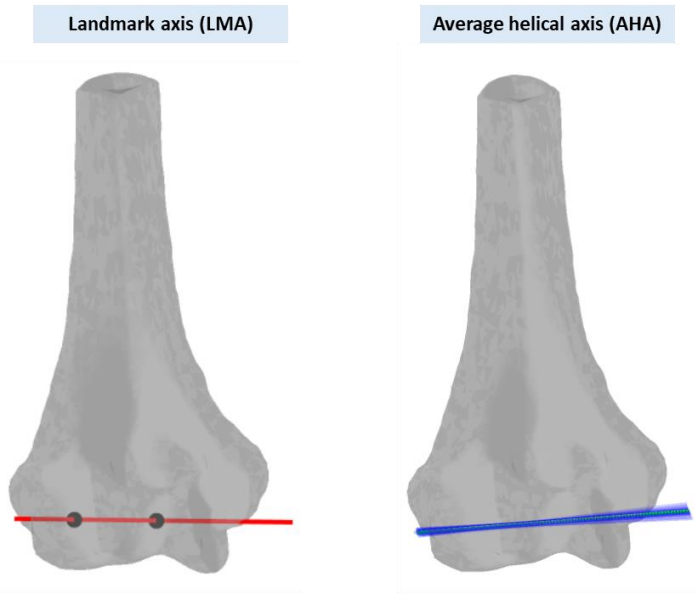

Figure 4: *Comparison of the landmark axis (LMA, red) and the average helical axis (AHA, green).*

Joint motion was modelled using a rotation axis defined by anatomical landmarks, referred to as the landmark axis (LMA). The LMA was established as the line connecting the geometric centres of the trochlea and capitellum on the distal humerus surface models (Fig. 4). Ulnohumeral articulation was selected because it is the primary driver of elbow flexion and extension, with the trochlea and capitellum providing a congruent surface for ulnar motion.

To validate the position and orientation of the LMA, the average helical axis (AHA) was derived per specimen. The AHA represents a single, average rotation axis for the entire flexion and extension motion, while finite helical axes (FHA) are instantaneous axes calculated at each flexion step. FHAs were calculated between the consecutive flexion steps and weighted by the corresponding instantaneous angle [12-14]. FHAs from full extension to 0 degrees were excluded from AHA computations due to known instability in screw axis estimations at low instantaneous angles [15]. All computations used open-source code developed by Ancillao [16]. AHA precision was assessed by the estimation error, defined by the variability among individual FHAs. Positional error was defined as the root mean square (RMS) of the orthogonal distances from each FHA to the AHA. The angular error was calculated as the RMS of directional deviations, defined as angles between the orientation vectors of individual FHAs and the AHA. [12]

The LMA's location and orientation were compared to those of the AHA. The primary outcomes were the translational and angular differences between the axes. These were defined as the minimal distance and the smallest angle between the axes. Mean and standard deviations (SD) of these differences were reported.

2.1.4 Ulnar pose accuracy

To assess the accuracy of simulated ulnar motion using the LMA and AHA, rotation angles derived from FHA analysis (Section 2.1.3) were applied to the neutral ulna pose (0° flexion) to generate predicted

poses across the flexion range. These simulated poses were then compared to each specimen's corresponding scanned ulna poses.

For each flexion angle, a transformation matrix was computed describing the rigid-body deviation between the scanned and simulated ulnae poses, with both expressed relative to the humerus. Translational error was defined as the displacement vector extracted from this matrix. Rotational error was derived by decomposing the rotational component into Euler angles in the clinical order: flexion/extension (z-axis), varus/valgus (x-axis), and internal/external rotation (y-axis). Errors were calculated per flexion angle and summarised using the mean and SD.

2.2 Bone impingement settings

Osseous impingement during elbow flexion and extension may occur at two distinct articular regions: the ulnohumeral and radiohumeral regions. Accordingly, bone impingement was defined as the volumetric intersection between the 3D surface models of the humerus and ulna, and the humerus and radius. Intersection volumes below 1 mm^3 were classified as noise and excluded. Bony contact was not anticipated during flexion and extension, except at terminal positions.

Total impingement volumes were calculated for each analysed position and plotted against the corresponding flexion angles. Exponential curves were fitted separately for flexion and extension phases, independently analysing intersections in the ulnohumeral and radiohumeral regions. To minimise the influence of measurement noise, only data points exceeding 20% of the maximum impingement volume were included in the curve-fitting process. This 20% threshold was determined through an initial trial-and-error approach, identifying a balance between excluding noise and retaining meaningful data. The first measured volume located beyond the intersection points of the fitted curves with the horizontal axis was used to determine the maximal flexion and extension angles, indicating the onset of impingement.

2.3 Simulating range of motion

To translate insights from the cadaveric model into a clinical context, additional bilateral upper extremity CT scans of ten adult patients (age range 25–54 years; 2 female) were retrospectively retrieved from the imaging database of the Department of Orthopaedics and Sports Medicine at Erasmus Medical Center. The included patients were clinically suspected of having restricted elbow flexion and extension due to underlying osseous impingement. Scans without sufficient visualisation of the humeral shaft were excluded. Clinical ROM data close to the CT scan date and before treatment were extracted from medical records.

Both the affected and contralateral humerus, ulna, and radius were segmented using Mimics software, as described in Section 2.1.1, and converted into 3D surface models using 3-Matic. The contralateral humerus was mirrored and rigidly aligned to the affected humerus, specifically to the correct positioning of the capitellum and trochlea. This enabled the transfer of anatomical landmarks for LMA definition onto the pathological side.

The flexion angle of the scanned pose was calculated as the angle between two anatomical planes: a humeral plane defined by the shaft vector and the LMA, and an ulnar plane through the ulnar styloid and the LMA. This angle was used to align the simulation, ensuring ulnar and radial ROM around

the LMA from 10° of hyperextension to 150° of flexion was covered in 1° increments. Each resulting position was analysed for osseous impingement to determine patient-specific ROM. Model-based ROM was compared to clinically recorded values using the absolute mean difference with corresponding SDs.

3 | Results

3.1 LMA versus AHA

The mean translational and angular differences between the LMA and AHA were 0.41 mm (SD: 0.22; range: 0.07-0.65 mm) and 2.76° (SD: 1.32; range: 1.20°-4.59°), respectively. Individual results are presented in Table 1. The positional and orientational errors associated with AHA estimations averaged 1.33 mm (SD: 1.55) and 2.70° (SD: 1.38), respectively. Appendix B includes the corresponding error values and FHA deviations for each specimen.

The mean instantaneous flexion angles calculated from neutral position to each intended target position are shown in Appendix C. Compared to the aimed flexion angles of 30°, 60°, 90°, and 120°, the mean measured values deviated on average by -11.1° (SD: 5.3), -13.3° (SD: 5.3), -11.4° (SD: 4.3), and -15.1° (SD:9.3), respectively.

	1	2	3	4	5	6	7	8	Mean (SD)
Translational difference (mm)	0.42	0.07	0.33	0.45	0.62	0.65	0.14	0.60	0.41 (0.22)
Angular difference (°)	4.59	3.27	4.03	1.38	1.20	1.27	3.39	2.99	2.76 (1.32)

Table 1: *Translational and angular differences between the landmark axis (LMA) and average helical axis (AHA).*

3.2 Accuracy of simulated ulnar motion

Translation and rotation errors of the simulated ulnar pose were evaluated for LMA- and AHA-based simulations. Deviations observed in individual specimens are presented in Appendix X. For translations (Fig. 6, Appendix D), deviations primarily occurred along the proximal-distal (y) and lateral-medial (z) axes. In the lateral-medial direction, the largest mean errors were observed at 90° flexion (AHA: -0.67 ± 1.58 mm, LMA: -0.24 ± 1.68 mm), directed medially. In the proximal-distal direction, LMA showed greater deviations at higher flexion angles, peaking at maximal flexion (-1.44 ± 0.72 mm), while AHA deviations remained smaller (-0.02 ± 0.52 mm at max flexion). In the anterior-posterior (x) direction, the greatest variability occurred at 60° (AHA: -0.26 ± 2.97 mm; LMA: -0.70 ± 3.14 mm), directed posteriorly.

For rotation (Fig. 7, Appendix D), errors in flexion-extension (z) direction remained low for both LMA- and AHA-based simulations, with deviations below 0.5° across all flexion

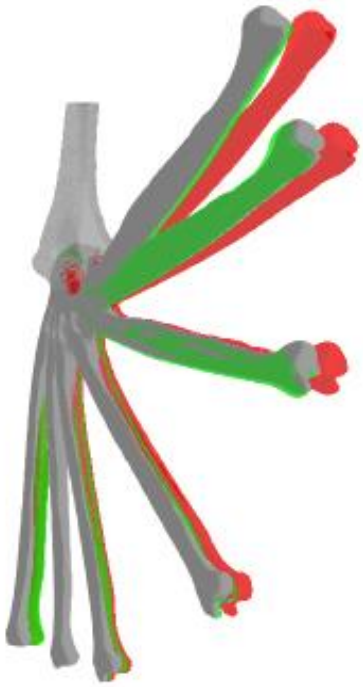

Figure 5: *Typical example illustrating the simulated ulnar poses for LMA-based (red) and AHA-based (green)*

angles. In the varus-valgus (x) direction, LMA showed the largest rotational deviation at maximum flexion (3.28°±3.90), compared to 0.86°±2.21 for AHA at 90°. In the internal/external (y) direction, AHA exhibited larger deviations than °LMA, with a maximum external rotation error of 1.28°±1.00, while LMA errors remained close to zero across the flexion range.

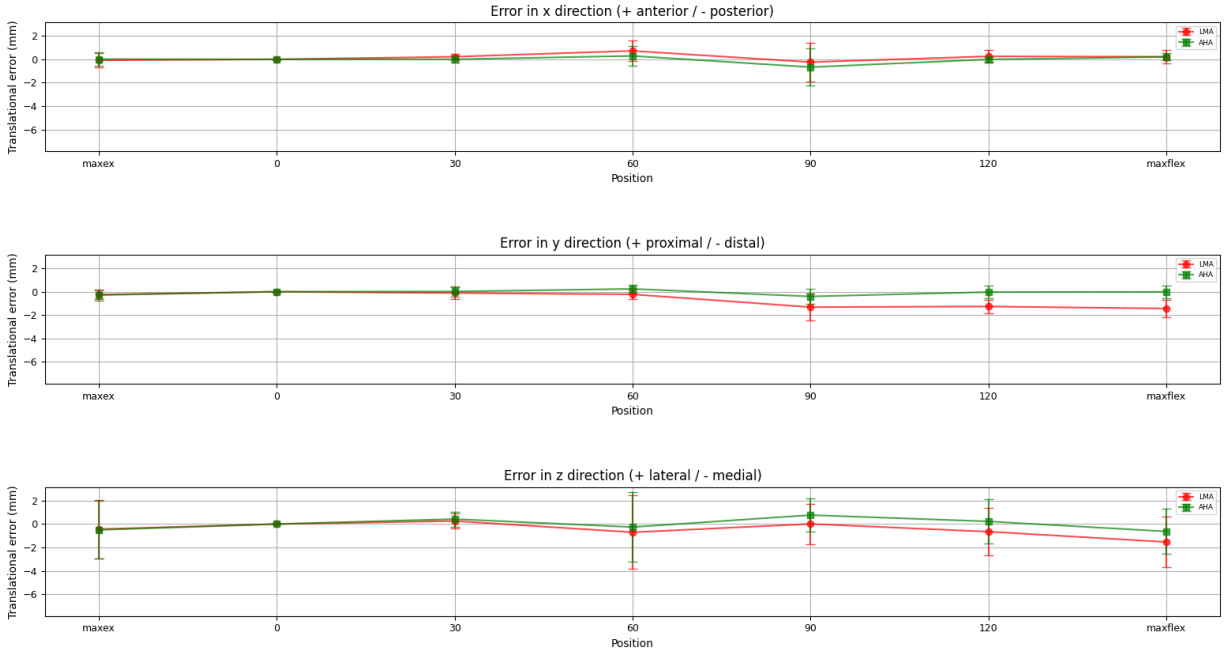

Figure 6: *Translational errors of the simulated ulnar pose in LMA- (red) and AHA-based (green) simulations, displayed across flexion angles. Errors are shown in x-direction (anterior-posterior), y-direction (proximal-distal), and x-direction (lateral-medial). Mean errors with standard deviations are indicated for each pose.*

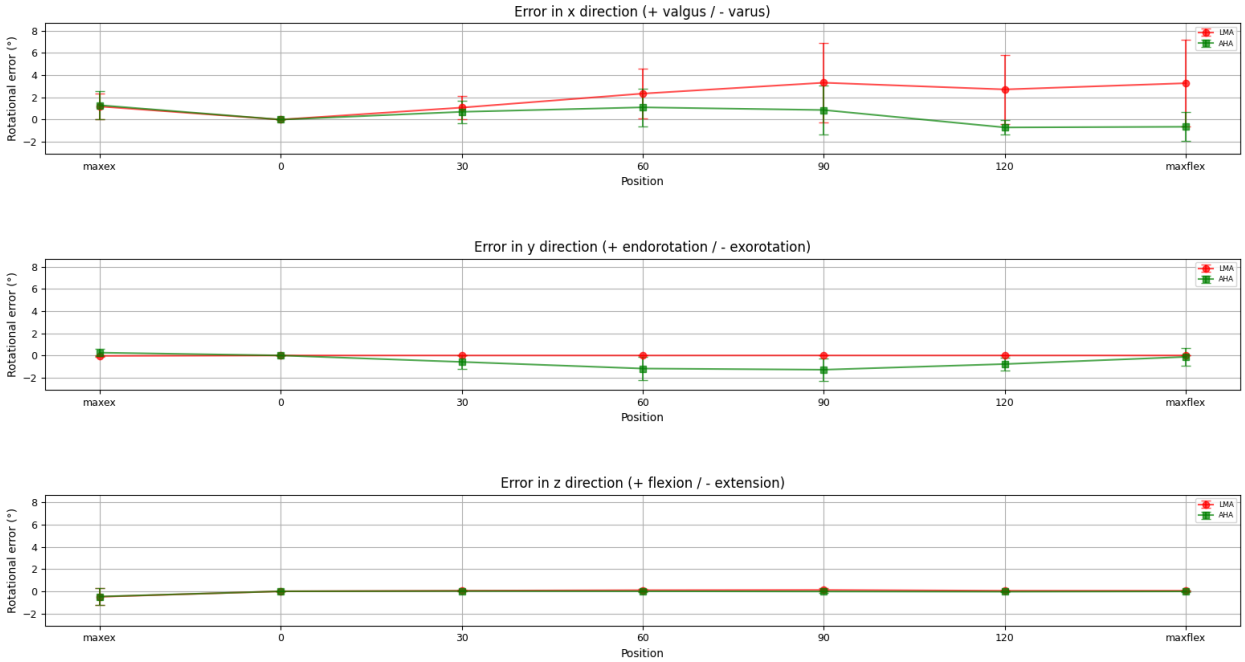

Figure 7: *Rotational errors of the simulated ulnar pose in LMA- (red) and AHA-based (green) simulations, displayed across flexion angles. Errors are shown in x-orientation (varus-valgus), y-orientation (internal-external), and x-orientation (flexion-extension). Mean errors with standard deviations (SD) are indicated for each pose.*

3.3 Range of motion estimations

3.3.1. Specimen terminal poses

All eight specimens reached their terminal extension poses without encountering osseous impingement within the ulnohumeral or radiohumeral joints. In contrast, flexion was restricted by impingement in three of the eight specimens, exclusively within the ulnohumeral region. Impingement occurred between the medial aspect of the trochlea and the medial margin of the greater sigmoid notch, initiating at 117° for specimen 1 (expected terminal flexion at 140°), 37° for specimen 5 (expected terminal flexion at 128°), and 83° for specimen 6 (expected terminal flexion at 144°). Specimen 5 additionally exhibited impingement involving the lateral margin of the greater sigmoid notch between 37° and 59°. Impingement volumes for these specimens are detailed in Appendix E. Notably, specimens 5 and 6 did not demonstrate an exponential increase in impingement volume during flexion. The highest recorded non-physiological volume measured was 152 mm^3. No impingement was detected in the radiohumeral joint between the humerus and radius before reaching the terminal position.

3.3.2. Patient terminal poses

Clinically measured and model-based ROM were compared across nine patients (Table 2, Fig. 8). For terminal extension poses, the model showed a mean absolute difference of 6.7° (SD: 4.3), with individual differences ranging from 5° of underestimation to 14° of overestimation. Six patients reached their clinically measured terminal extension poses without evidence of osseous impingement. In three patients, the model underestimated the terminal extension poses, specifically for patient 5 (clinical: 0°, model: 4°), patient 6 (clinical: 0°, model: 2°), and patient 9 (clinical: 10°, model: 15°). In patients 5 and 6, osseous impingement was detected within the ulnohumeral region between the olecranon fossa and the olecranon process. This impingement was characterised by a progressively increasing impingement volume, following an exponential pattern as extension progressed. In patient 9, osseous impingement was observed in the radiohumeral region, with the impingement volume increasing exponentially between the superior surface of the radial head and the inferior aspect of the capitellum.

For terminal flexion poses, the mean absolute difference was 14.2° (SD: 15.6°), with deviations varying between 44° of underestimation to 31° of overestimation. Five patients reached their clinically measured terminal flexion poses without encountering osseous impingement. In four patients, the model's predictions underestimated the clinically measured values. Specifically, for patient 2 (clinical: 110°, model: 93°), patient 5 (clinical: 85°, model: 83°), patient 8 (clinical: 125°, model: 123°), and patient 9 (clinical: 120°, model: 76°). For patients 5 and 8, impingement was identified within the radiohumeral region, occurring between the anterior-superior surface of the radial head and the anterior aspect of the

	1	2	3	4	5	6	7	8	9
Clinical terminal extension (°)	10	30	40	20	0	0	10	30	10
Model terminal extension (°)	4	16	28	13	4	2	6	24	15
Clinical terminal flexion (°)	95	110	80	100	85	120	90	125	120
Model terminal flexion (°)	100	93	80	123	83	123	121	122	76

Table 2: *Comparison of clinically measured and model-based terminal extension and flexion angles across nine patients.*

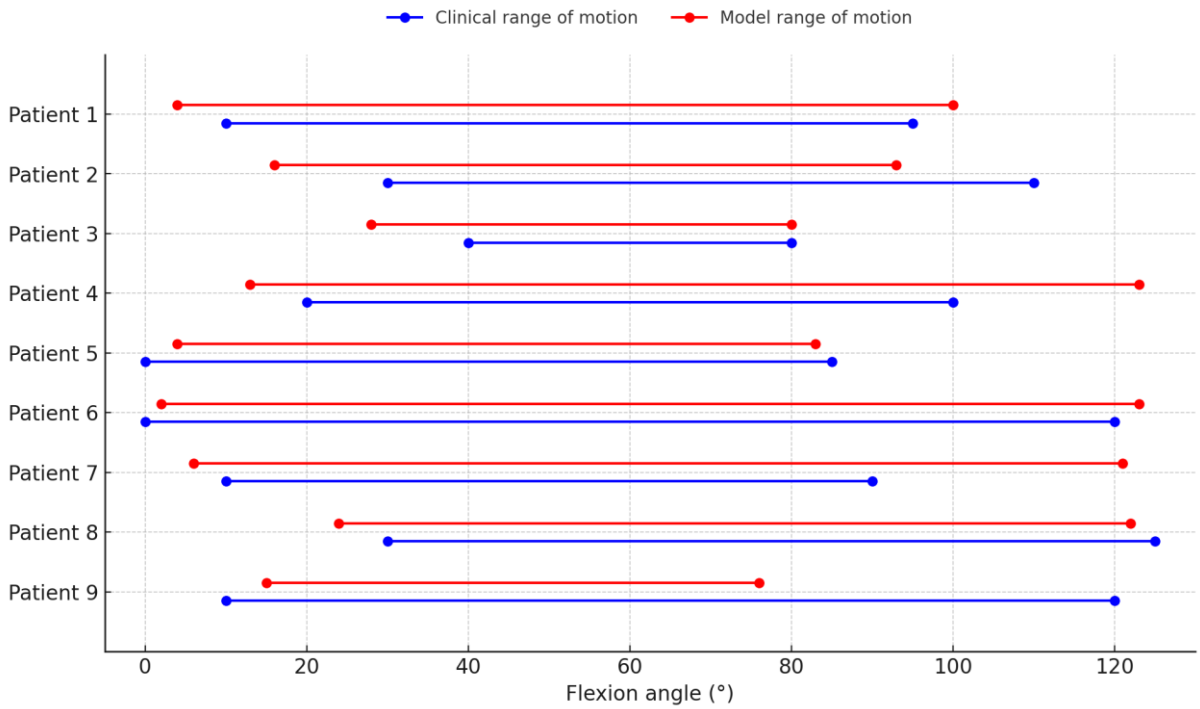

Figure 8: : *Comparison of clinically measured (blue) and model-based (red) range of motion across nine patients.*

capitellum. In patients 2 and 9, impingement occurred within the ulnohumeral region. Patient 2 exhibited impingement between the anterior aspect of the trochlea and the coronoid process. In patient 9, impingement was initially observed between the medial aspect of the trochlea and the medial margin of the greater sigmoid notch, occurring between 76° and 127° of flexion. Beyond 127°, impingement shifted to occur between the coronoid fossa and the coronoid process. For all four patients, impingement volumes showed an exponential increase with increasing flexion.

An overview of all observed ulnohumeral and radiohumeral impingement volumes across the full ROM for all patients is presented in Appendix F.

4 | Discussion

4.1 Principal findings

This study aimed to introduce and validate a computational model for simulating patient-specific elbow flexion and extension using 3D bone models of the humerus, ulna and radius retrieved from a single CT scan. By isolating the osseous component of joint motion, the model seeks to provide a patient-specific, quantitative method for assessing the contribution of bony anatomy to ROM restrictions, thereby offering a clinically feasible alternative to dynamic imaging techniques.

The first objective of this study was to assess whether elbow flexion and extension can be accurately modelled as a rotation around a single, automatically placed LMA. Comparison between the LMA and the kinematically derived AHA demonstrated that the LMA closely approximates the AHA, with positional (1.33±1.55 mm) and angular (2.70±1.38°) deviations well within the natural variability of the

FHAs. The FHA variability found is consistent with the variability reported by Bottlang et al. [17] (1.4 to 2.0 mm in translation and 2.6° to 5.7° in orientation), supporting the use of the LMA as a valid representation of the elbow's axis of rotation. Bottlang et al. concluded that these deviations are clinically irrelevant due to their minimal magnitude relative to the total arc of elbow motion and their consistent pattern across ROM. This reinforces the concept that the elbow, while not behaving as a purely uniaxial hinge, can be effectively modelled using a fixed axis.

However, the model's ability to simulate ulnohumeral motion revealed that LMA-based simulations were more susceptible to systematic errors, which progressively increased at higher flexion angles. These errors were characterised by distal translation, lateral drift, and valgus deviation. Such a progressive error pattern suggests a cumulative effect of small axis misalignments originating from the neutral 0° reference. Specifically, this pattern aligns with a lateral-medial misalignment of the LMA, potentially caused by medial elevation and/or lateral depression of the axis. This tilting would direct the ulna along an increasingly oblique path during flexion, resulting in the observed progressive displacement and angular deviation.

Misalignment of the LMA may stem from two sources: incorrect estimation of the rotation axis itself or inaccuracies in the automatic landmark placement of anatomical landmarks. However, given that prior research consistently identifies the centres of the trochlea and capitellum as the optimal axis location [17-20], a fundamental axis misplacement seems unlikely. The more plausible explanation is variability in landmark placement. Negrillo-Cardenas et al. [9] reported a placement error ranging from 0.5 and 2.1 mm for the capitellum and 0.25 to 3.0 mm for the trochlea. This variability aligns with the deviations observed in the simulated ulnar poses, where the magnitude and direction of positional and angular deviations varied across specimens while maintaining a consistent overall pattern. These findings indicate that even minor inaccuracies in landmark placement can accumulate, resulting in systematic deviations during flexion simulation.

From a clinical perspective, the observed simulation errors are unlikely to impact the detection of major osseous motion restrictions, supporting the validity of using the LMA as a patient-specific approximation of elbow rotation in flexion and extension.

The second objective of this study was to evaluate the model's capability in predicting elbow flexion and extension ROM using the LMA as the axis of rotation. Since the model exclusively simulates osseous constraints, underestimation of model-based ROM relative to clinical measurements likely indicates erroneous detection of impingement, reflecting model inaccuracies. Conversely, overestimation may result from clinically observed soft-tissue restrictions not represented in the osseous-only model. Clinical ROM assessments themselves are inherently subject to variability; goniometric measurements of elbow motion exhibit intra- and interobserver differences ranging between 5.2° and 6.6° [21]. Model deviations within this margin are therefore unlikely to be clinically relevant, as was the case for all underestimated extension poses and the terminal flexion poses of patients 5 and 8.

This leaves clinically relevant deviation at terminal flexion poses for patients 2 and 9. In patient 2, the model underestimated end-range flexion by 17°, with apparent impingement between the anterior trochlea and the coronoid process. This suggests a distally directed misalignment of the LMA, causing the simulated ulna to follow a lower arc and make premature anterior contact. In patient 9, the model underestimated flexion by 44°, with apparent impingement between the trochlea and greater

sigmoid notch, consistent with the patterns observed in specimen ROM estimations. This error aligns the model's tendency for distal translation, lateral drift, and valgus deviation of the ulna, indicating tilting in the lateral-medial direction as described earlier.

These findings demonstrate that while the model effectively identifies locations of osseous impingement, its specificity is limited by sensitivity to minor LMA misalignments. False-positive impingement occurred in the highly congruent ulnohumeral region, where small misalignments quickly lead to anatomically implausible contact. Consequently, clinicians cannot rely solely on the calculated terminal poses but must visually confirm simulated impingement locations to distinguish true ROM restrictions from false positives.

4.2 Strengths and limitations

To our knowledge, this was the first study to explore single CT-based 3D computational modelling, incorporating automatically placed anatomical landmarks, to simulate patient-specific elbow flexion and extension. This study presents several key strengths. First, automatically placed anatomical landmarks provide a standardised and reproducible method for defining local coordinate systems and rotation axes, minimising user-dependent variability and enhancing methodological consistency across specimens. Second, using a clear biomechanical framework, the model was validated against a kinematically derived reference axis. This allowed a robust assessment of axis accuracy, supported by quantitative analysis of positional and orientational deviations, thereby providing the model's ability to replicate joint motion. Third, this model enables isolated assessment of osseous restrictions based on standard clinical imaging, offering direct clinical applicability without requiring specialised dynamic imaging techniques.

Several limitations should also be considered when interpreting the findings of this study. First, the LMA was validated using cadaveric specimens without known ROM restrictions. While this allowed evaluation of axis accuracy under anatomically preserved and biomechanically controlled conditions, the applicability of the results to pathological elbows with osseous deformities remains untested. Second, although loose bodies are a recognised cause of mechanical blockage in the elbow [6], they were not included in the impingement analysis due to the difficulty of reliably predicting their movement during flexion and extension. This exclusion may lead to a slight underestimation of ROM limitations in cases where large, fixed loose bodies cause obstruction. However, the impact of mobile loose bodies is expected to be minimal, as they typically shift position without consistently restricting motion. Third, the transfer of anatomical landmarks from the contralateral side assumed bilateral symmetry. Although this method is practical and commonly used in clinical settings, it may introduce minor inaccuracies in cases of asymmetry caused by pathological osseous conditions (e.g. osteophytes, malunions, or osteoarthritis). Finally, the small sample size of eight cadaveric specimens and ten patient cases may limit generalizability. Nevertheless, the diverse anatomical characteristics within the cohorts provide a solid foundation for the model's initial validation.

4.3 Clinical applicability and future perspective

The model introduced in this study provides patient-specific assessments of elbow ROM using standard CT imaging, supporting both patient education and clinical decision-making. For patients without osseous impingement, it emphasises the role of soft tissue restrictions, reinforcing the value of

conservative management. Conversely, detecting clear osseous impingement can guide clinicians towards surgical intervention.

Further research is needed to investigate whether the landmark placement errors are consistent and systematic across specimens. If systematic errors are confirmed, the anatomical definition of the capitellum and trochlea centres may require refinement. Improved landmark positioning could reduce axis alignment errors, enhancing ROM predictions. Should alignment alone prove insufficient, restricting impingement detection to anatomically relevant regions, such as the olecranon and coronoid fossae, may further reduce false-positive findings and increase the model's clinical reliability.

5 | Conclusion

This study demonstrated that elbow flexion and extension can be simulated based on automatically placed anatomical landmarks on patient-specific 3D bone models derived from single CT scans. The LMA showed close agreement with the kinematically derived AHA, supporting its validity for modelling ulnohumeral rotation. Model-predicted ROM showed good agreement with clinically measured ROM, suggesting that this method provides a reliable estimation of osseous motion restrictions. These findings support the feasibility of patient-specific 3D computational modelling to assess the osseous contribution to elbow motion restriction based on standard clinical imaging, offering a practical and low-radiation alternative to dynamic imaging techniques. Future refinements should aim to increase model specificity by limiting impingement detection to anatomical regions where bone contact is expected to restrict joint motion, further enhancing clinical applicability.

6 | References

1. Morrey BF, Askew LJ, Chao EY. A biomechanical study of normal functional elbow motion. J Bone Joint Surg Am. 1981;63(6):872-7.
2. Sardelli M, Tashjian RZ, MacWilliams BA. Functional elbow range of motion for contemporary tasks. J Bone Joint Surg Am. 2011;93(5):471-7.
3. Adolfsson L. Post-traumatic stiff elbow. EFORT Open Rev. 2018;3(5):210-6.
4. Patino JM, Saenz VP. Stiff Elbow. 2024.
5. Morrey BF. The posttraumatic stiff elbow. Clin Orthop Relat Res. 2005(431):26-35.
6. Siemensma MF, van der Windt AE, van Es EM, Colaris JW, Eygendaal D. Management of the stiff elbow: a literature review. EFORT Open Rev. 2023;8(5):351-60.
7. Seah RB, Mak WK, Bryant K, Korlaet M, Dwyer A, Bain GI. Four-dimensional computed tomography scan for dynamic elbow disorders: recommendations for clinical utility. JSES Int. 2022;6(1):182-6.
8. Wong MT, Wiens C, Kuczynski M, Manske S, Schneider PS. Four-dimensional computed tomography: musculoskeletal applications. Can J Surg. 2022;65(3):E388-E93.
9. Negrillo-Cardenas J, Jimenez-Perez JR, Canada-Oya H, Feito FR, Delgado-Martinez AD. Automatic detection of landmarks for the analysis of a reduction of supracondylar fractures of the humerus. Med Image Anal. 2020;64:101729.
10. van Loon DFR, van Es EM, Eygendaal D, Veeger D, Colaris JW. Automatic identification of radius and ulna bone landmarks on 3D virtual models. Comput Biol Med. 2024;179:108891.
11. Wu G, van der Helm FC, Veeger HE, Makhsous M, Van Roy P, Anglin C, et al. ISB recommendation on definitions of joint coordinate systems of various joints for the reporting of human joint motion--Part II: shoulder, elbow, wrist and hand. J Biomech. 2005;38(5):981-92.
12. Spoor CW, Veldpaus FE. Rigid body motion calculated from spatial co-ordinates of markers. J Biomech. 1980;13(4):391-3.
13. Woltring HJ. Estimation of the trajectory of the instantaneous centre of rotation in planar biokinematics. J Biomech. 1990;23(12):1273-4.
14. Ehrig RM, Heller MO. On intrinsic equivalences of the finite helical axis, the instantaneous helical axis, and the SARA approach. A mathematical perspective. J Biomech. 2019;84:4-10.
15. Woltring HJ, Huiskes R, de Lange A, Veldpaus FE. Finite centroid and helical axis estimation from noisy landmark measurements in the study of human joint kinematics. J Biomech. 1985;18(5):379-89.
16. Ancillao A. The helical axis of anatomical joints: calculation methods, literature review, and software implementation. Med Biol Eng Comput. 2022;60(7):1815-25.
17. Bottlang M, Madey SM, Steyers CM, Marsh JL, Brown TD. Assessment of elbow joint kinematics in passive motion by electromagnetic motion tracking. J Orthop Res. 2000;18(2):195-202.
18. London JT. Kinematics of the elbow. J Bone Joint Surg Am. 1981;63(4):529-35.
19. Goto A, Moritomo H, Murase T, Oka K, Sugamoto K, Arimura T, et al. In vivo elbow biomechanical analysis during flexion: three-dimensional motion analysis using magnetic resonance imaging. J Shoulder Elbow Surg. 2004;13(4):441-7.
20. Veeger HE, Yu B, An KN, Rozendal RH. Parameters for modeling the upper extremity. J Biomech. 1997;30(6):647-52.
21. Armstrong AD, MacDermid JC, Chinchalkar S, Stevens RS, King GJ. Reliability of range-of-motion measurement in the elbow and forearm. J Shoulder Elbow Surg. 1998;7(6):573-80.

Appendix A: Fixation setup cadaveric scans

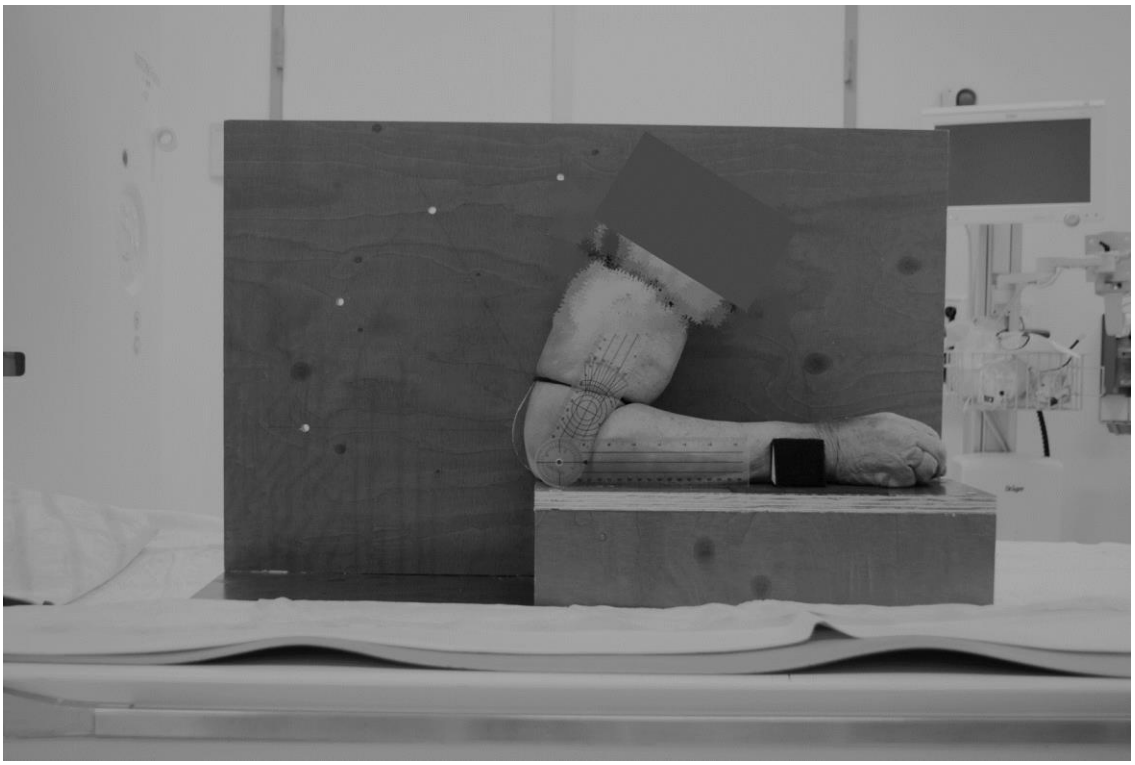

Figure A1: Side-view of the fixation setup with the elbow in 120° of flexion.

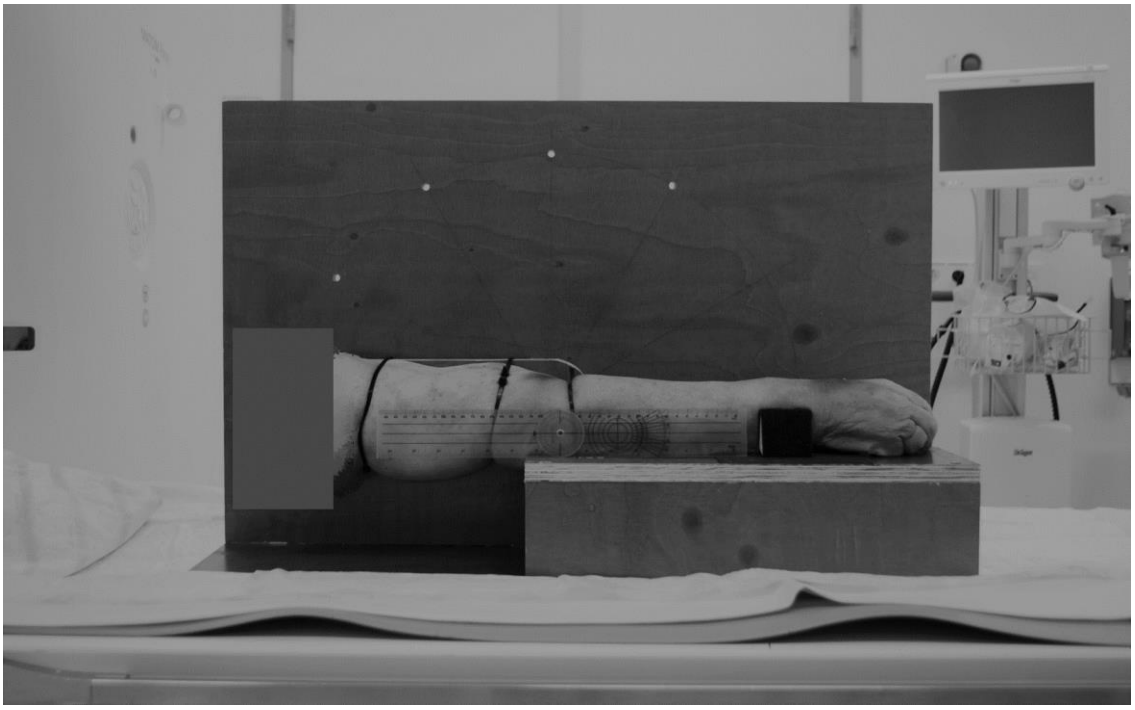

Figure A2: Side-view of the fixation setup with the elbow in 0° of flexion.

Appendix B: FHA deviations

	1	2	3	4	5	6	7	8	Mean (SD)
RMSE distance (mm)	0.65	0.39	0.25	0.36	1.24	0.68	2.35	4.71	1.33 (1.55)
RMSE angle (°)	2.77	2.06	3.09	1.31	1.33	2.06	3.42	5.55	2.70 (1.30)

Table B1: *Positional and angular FHA deviations across specimens.*

Appendix C: Instantaneous angle

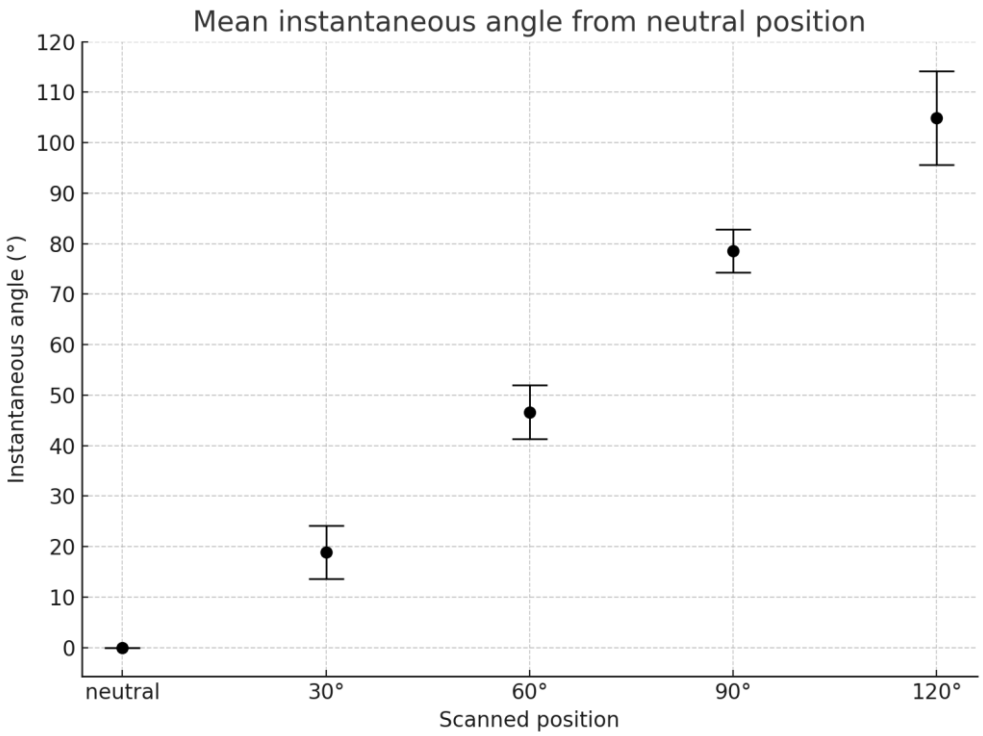

***Figure C1**: Mean instantaneous angle form neutral position (0°) to each scanned position. Error bars indicate standard deviation.*

Specimen	Max. ex.	30	60	90	120	Max. flex.
1	-6.19	26.24	52.28	82.68	116.71	139.18
2	-10.99	13.98	42.75	71.98	93.64	105.95
3	-6.46	16.78	43.53	77.93	116.25	138.71
4	-4.42	25.84	55.65	85.95	110.05	125.79
5	-1.52	16.31	44.27	75.65	95.92	109.85
6	-3.26	22.31	48.58	78.47	105.77	134.52
7	-3.07	16.93	46.77	79.53	106.05	132.65
8	-14.08	12.46	39.43	76.38	95.15	123.64
Mean	-	**18.86**	**46.66**	**78.57**	**104.94**	-
SD	-	**5.27**	**5.33**	**4.3**	**9.25**	-

***Table C1:** Instantaneous angle from neutral position (0°) to each scanned position per specimen. Last two rows present the mean and standard deviation (SD) across all specimens.*

Appendix D: Ulnar pose accuracy

Method	Position	X mean ± SD	Y mean ± SD	Z mean ± SD
AHA	Max. ex.	0.02 ± 0.56	-0.29 ± 0.47	-0.50 ± 2.48
	0	0.00 ± 0.00	0.00 ± 0.00	0.00 ± 0.00
	30	0.01 ± 0.29	0.02 ± 0.46	0.43 ± 0.64
	60	0.29 ± 0.86	0.24 ± 0.35	-0.26 ± 2.97
	90	-0.67 ± 1.58	-0.41 ± 0.62	0.77 ± 1.40
	120	-0.01 ± 0.21	-0.03 ± 0.53	0.23 ± 1.88
	Max. flex.	0.21 ± 0.30	-0.02 ± 0.52	-0.63 ± 1.94
LMA	Max. ex.	-0.08 ± 0.61	-0.25 ± 0.39	-0.44 ± 2.49
	0	0.00 ± 0.00	0.00 ± 0.00	0.00 ± 0.00
	30	0.22 ± 0.27	-0.12 ± 0.53	0.26 ± 0.66
	60	0.72 ± 0.86	-0.23 ± 0.39	-0.70 ± 3.14
	90	-0.24 ± 1.68	-1.32 ± 1.16	0.01 ± 1.74
	120	0.26 ± 0.55	-1.27 ± 0.57	-0.65 ± 2.01
	Max. flex.	0.22 ± 0.57	-1.44 ± 0.72	-1.53 ± 2.17

Table D1: *Translational errors of the simulated ulnar pose in LMA- and AHA-based simulations across flexion angles. Errors are shown in x-direction (anterior-posterior), y-direction (proximal-distal), and x-direction (lateral-medial). Mean errors with standard deviations(SD) are indicated for each pose.*

Method	Position	X mean ± SD	Y mean ± SD	Z mean ± SD
AHA	Max. ex.	1.30° ± 1.23	0.25° ± 0.33	-0.48° ± 0.76
	0	0.00° ± 0.00	0.00° ± 0.00	0.00° ± 0.00
	30	0.70° ± 1.00	-0.58° ± 0.60	0.03° ± 0.04
	60	1.10° ± 1.70	-1.18° ± 1.02	0.01° ± 0.08
	90	0.86° ± 2.21	-1.28° ± 1.00	-0.01° ± 0.13
	120	-0.71° ± 0.66	-0.78° ± 0.56	-0.03° ± 0.08
	Max. flex.	-0.65° ± 1.29	-0.13° ± 0.79	-0.01° ± 0.06
LMA	Max. ex.	1.19° ± 1.18	-0.04° ± 0.08	-0.49° ± 0.75
	0	0.00° ± 0.00	0.00° ± 0.00	0.00° ± 0.00
	30	1.08° ± 1.03	0.00° ± 0.00	0.05° ± 0.07
	60	2.34° ± 2.22	0.00° ± 0.00	0.10° ± 0.14
	90	3.32° ± 3.56	0.00° ± 0.01	0.12° ± 0.15
	120	2.72° ± 3.10	0.00° ± 0.00	0.05° ± 0.04
	Max. flex.	3.28° ± 3.90	0.00° ± 0.01	0.05° ± 0.04

Table D2: *Rotational errors of the simulated ulnar pose in LMA- and AHA-based simulations across flexion angles. Errors are shown in x-orientation (varus-valgus), y-orientation (internal-external), and x-orientation (flexion-extension). Mean errors with standard deviations(SD) are indicated for each pose.*

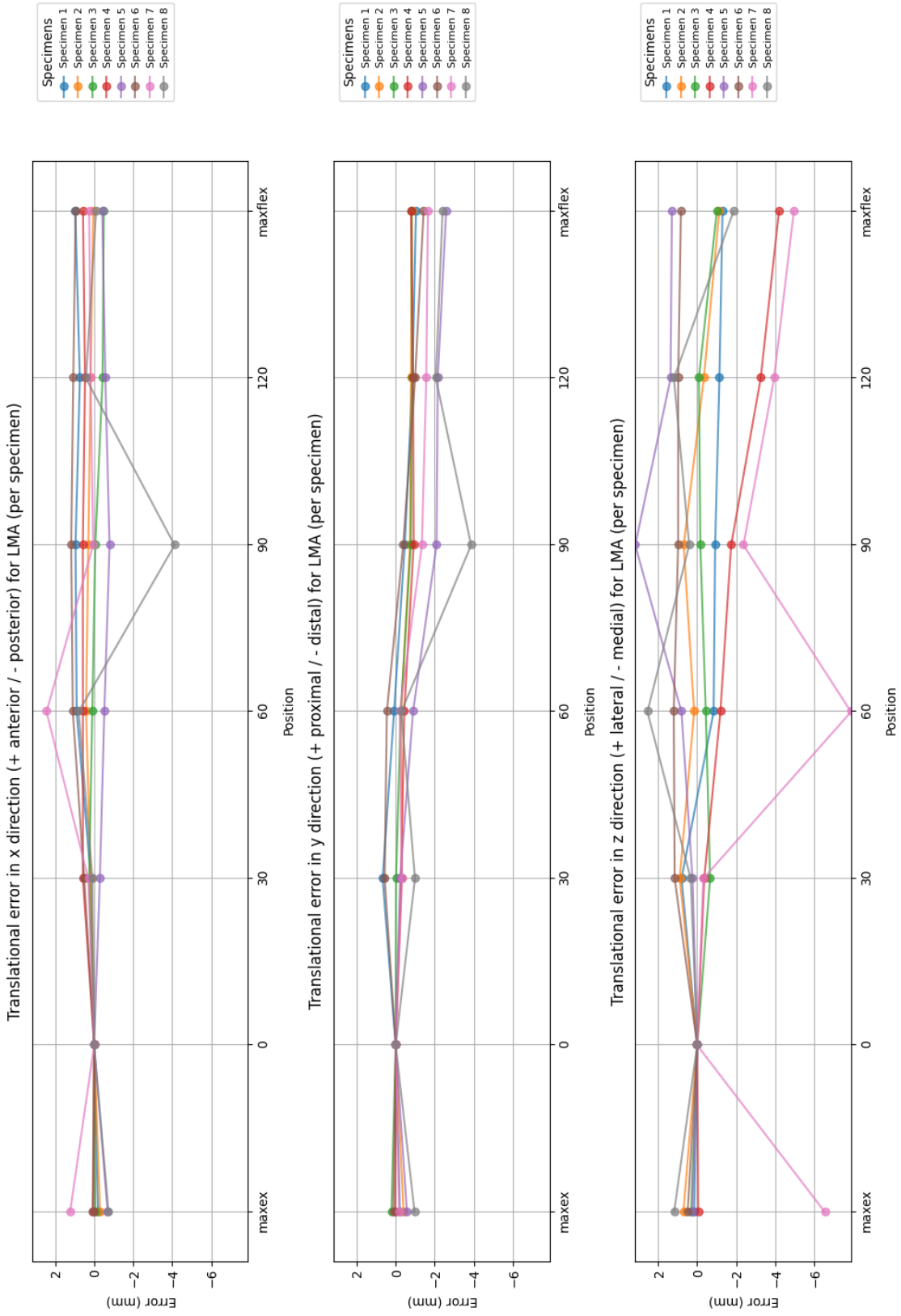

Figure D1: *Translational errors of the simulated ulnar pose in LMA-based simulations across flexion angles per specimen. Errors are shown in x-direction (anterior-posterior), y-direction (proximal-distal), and x-direction (lateral-medial).*

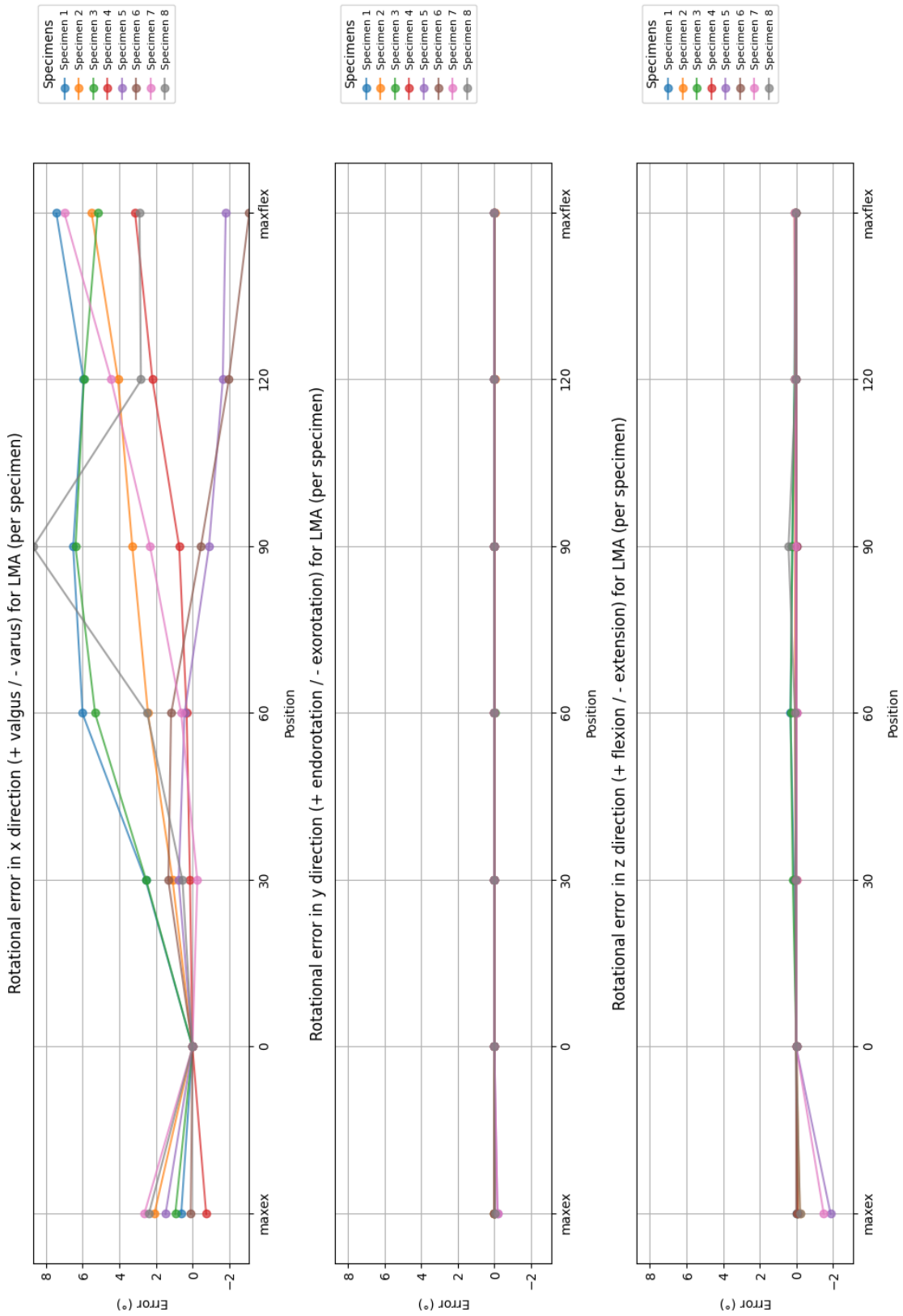

Figure D2: *Rotational errors of the simulated ulnar pose in LMA-based simulations across flexion angles per specimen. Errors are shown in x-orientation (varus-valgus), y-orientation (internal-external), and x-orientation (flexion-extension).*

Appendix E: Specimen-specific range of motion diagrams

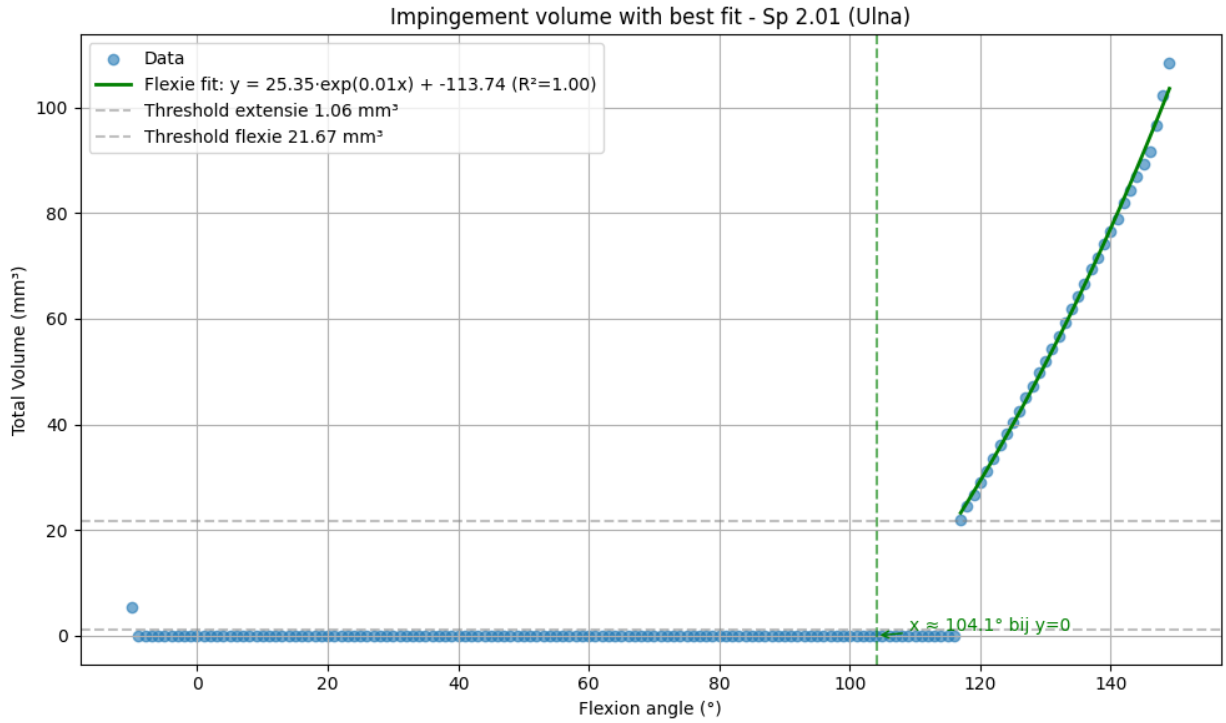

Figure E1: *Detected impingement volume (blue points) versus the flexion angle for the ulnohumeral region of specimen 1.An exponential fit identifies the onset of impingement (vertical dashed line).*

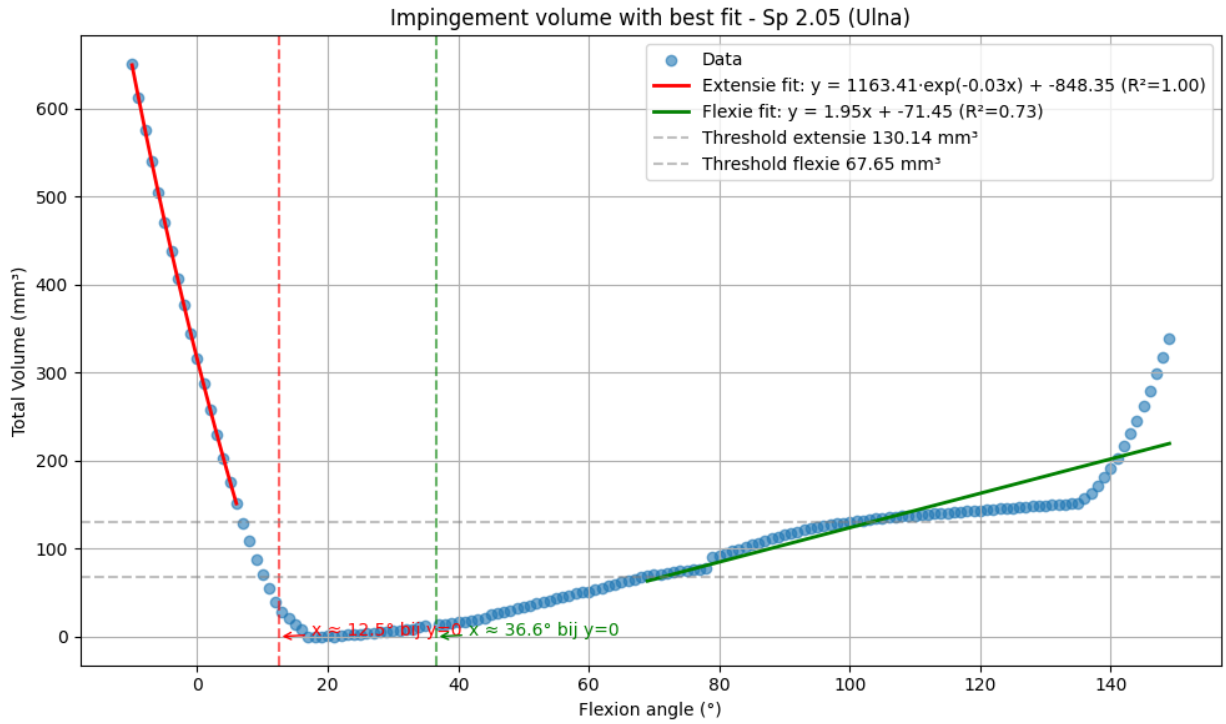

Figure E2: *Detected impingement volume (blue points) versus the flexion angle for the ulnohumeral region of specimen 5.An exponential fit identifies the onset of impingement (vertical dashed line).*

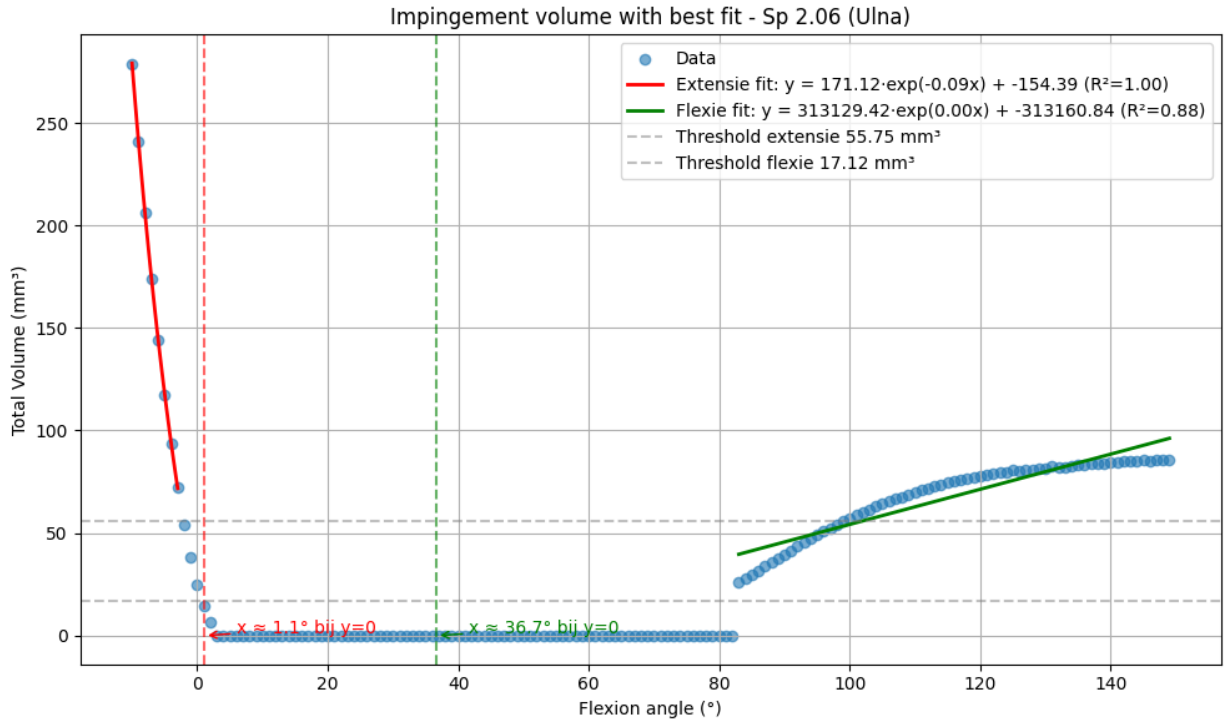

Figure E3: *Detected impingement volume (blue points) versus the flexion angle for the ulnohumeral region of specimen 1.An exponential fit identifies the onset of impingement (vertical dashed line).*

Appendix F: Patient-specific range of motion diagrams

Patient 1

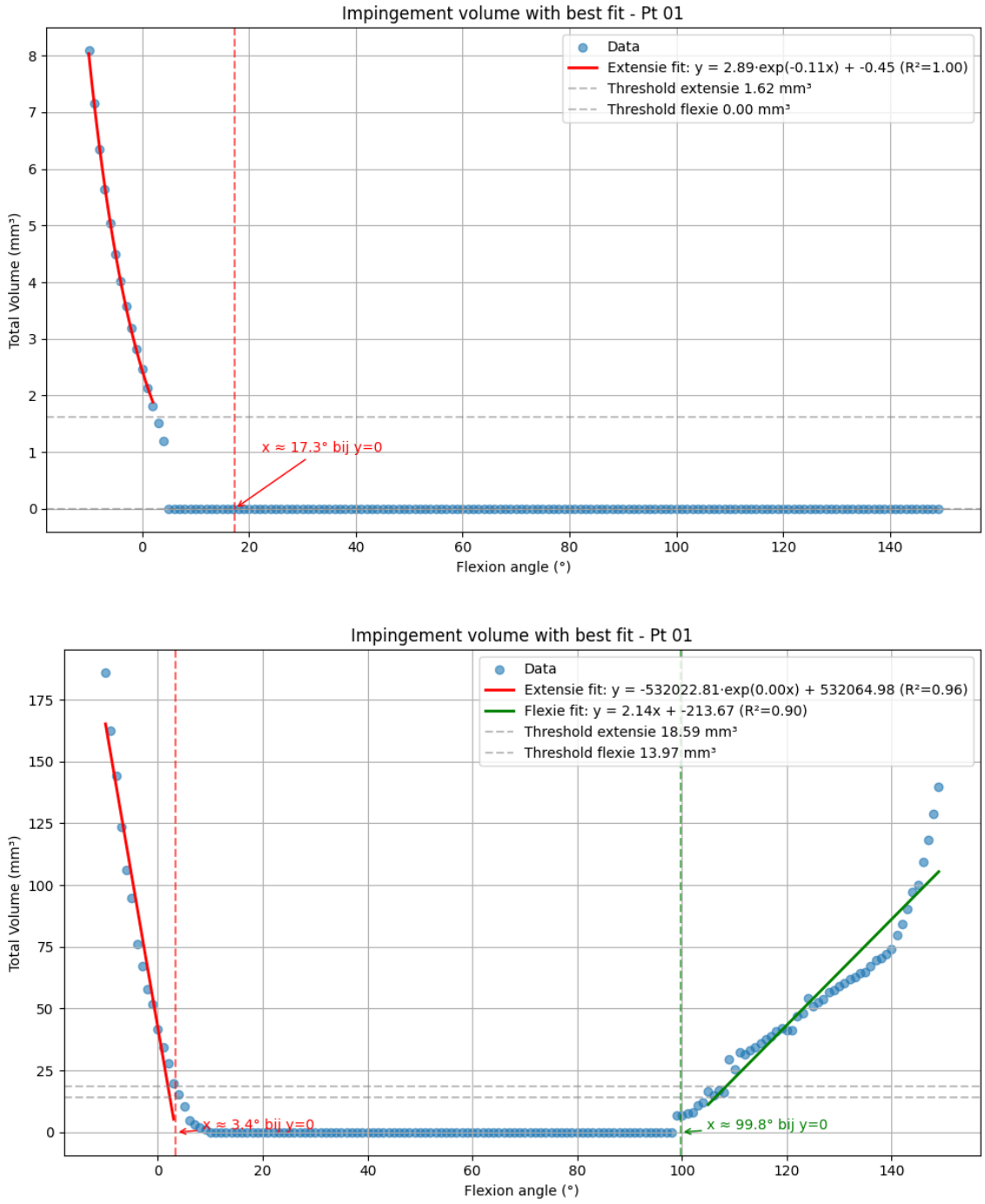

Figure F1: *Detected impingement volume (blue points) versus the flexion angle for the radiohumeral region (top) and ulnohumeral region (bottom) of patient 1. The exponential fits identify the onset of impingement (vertical dashed line).*

Patient 2

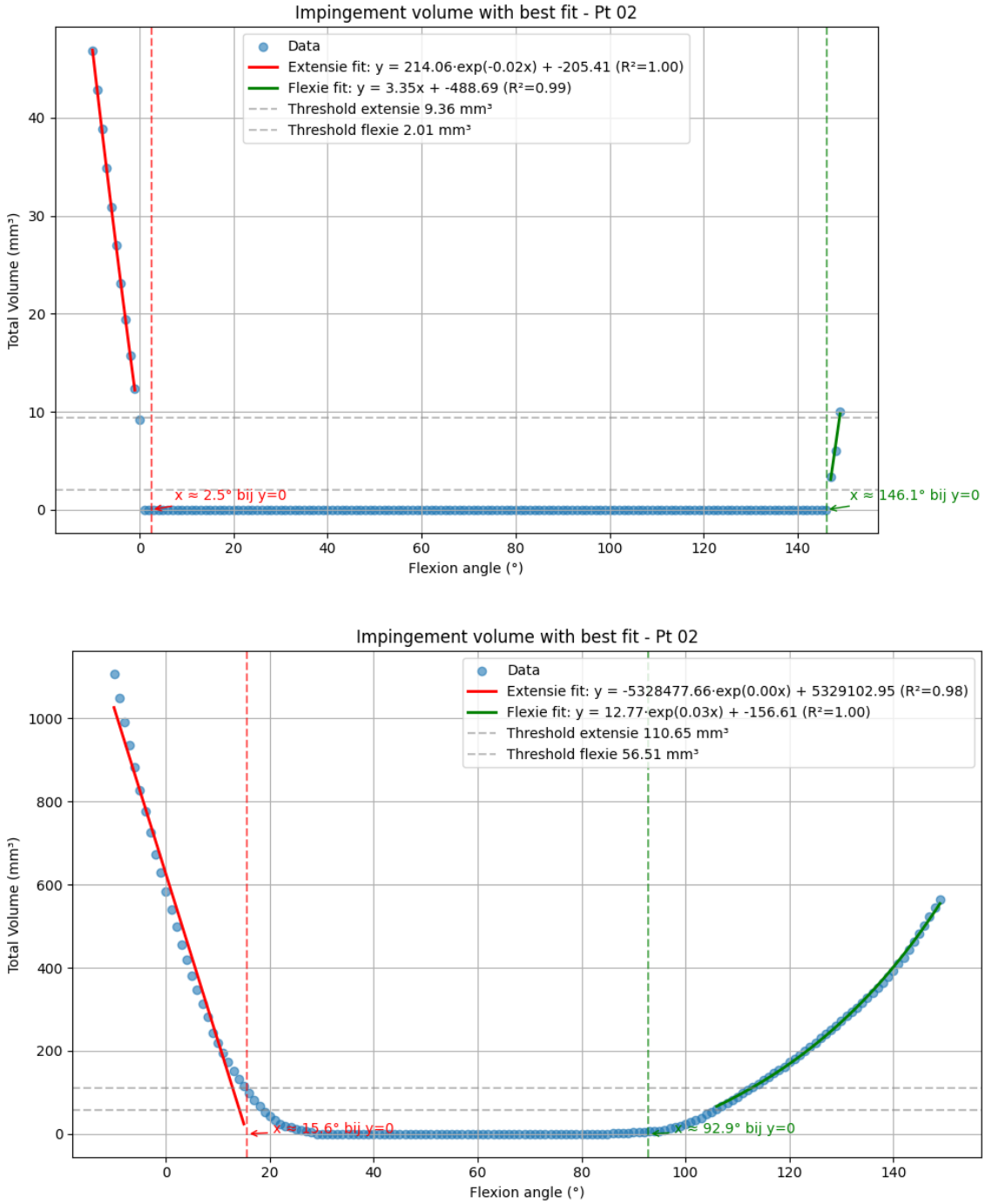

Figure F2: *Detected impingement volume (blue points) versus the flexion angle for the radiohumeral region (top) and ulnohumeral region (bottom) of patient 2. The exponential fits identify the onset of impingement (vertical dashed line).*

Patient 3

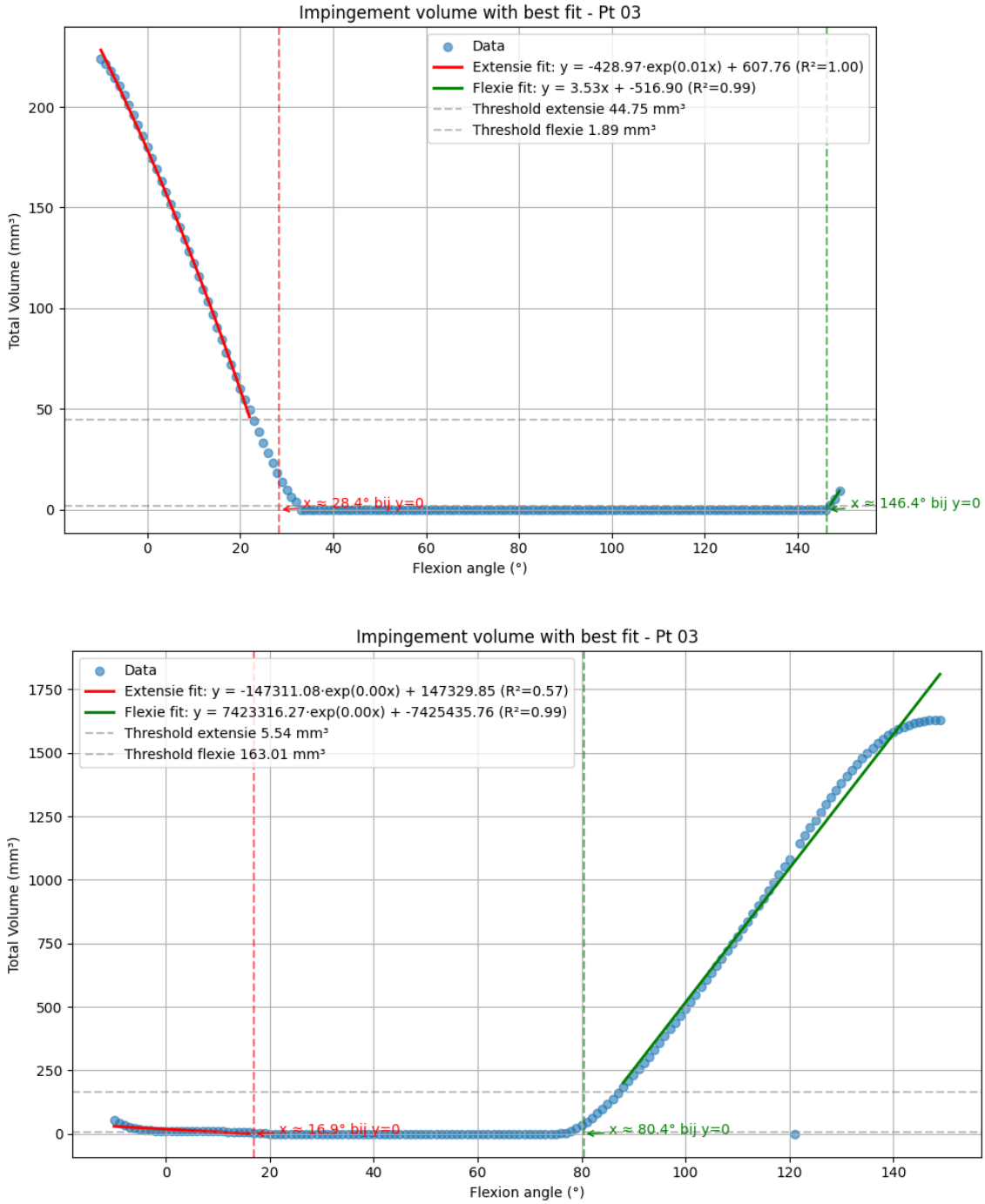

Figure F3: *Detected impingement volume (blue points) versus the flexion angle for the radiohumeral region (top) and ulnohumeral region (bottom) of patient 3. The exponential fits identify the onset of impingement (vertical dashed line).*

Patient 4

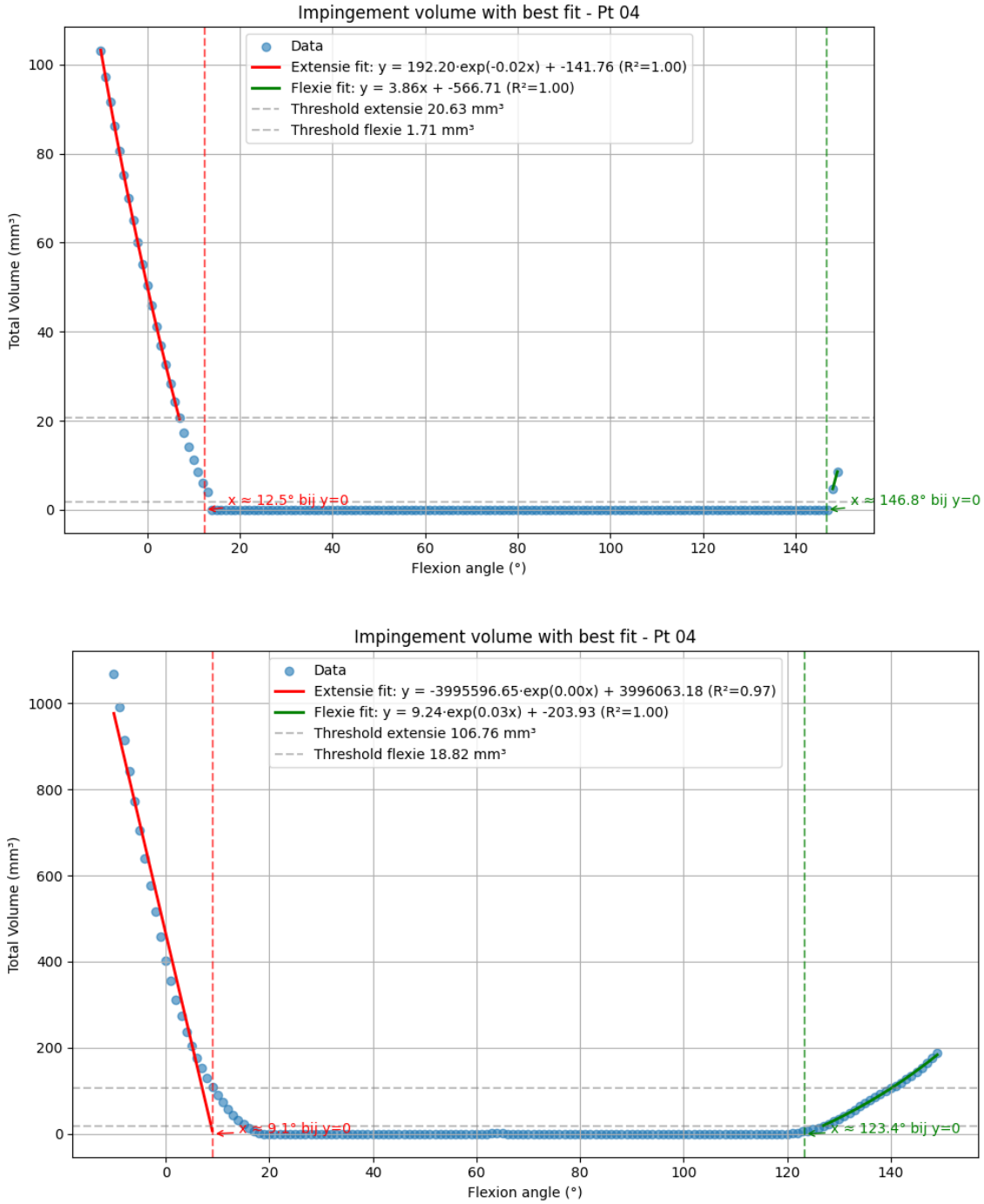

Figure F4: *Detected impingement volume (blue points) versus the flexion angle for the radiohumeral region (top) and ulnohumeral region (bottom) of patient 4. The exponential fits identify the onset of impingement (vertical dashed line).*

Patient 5

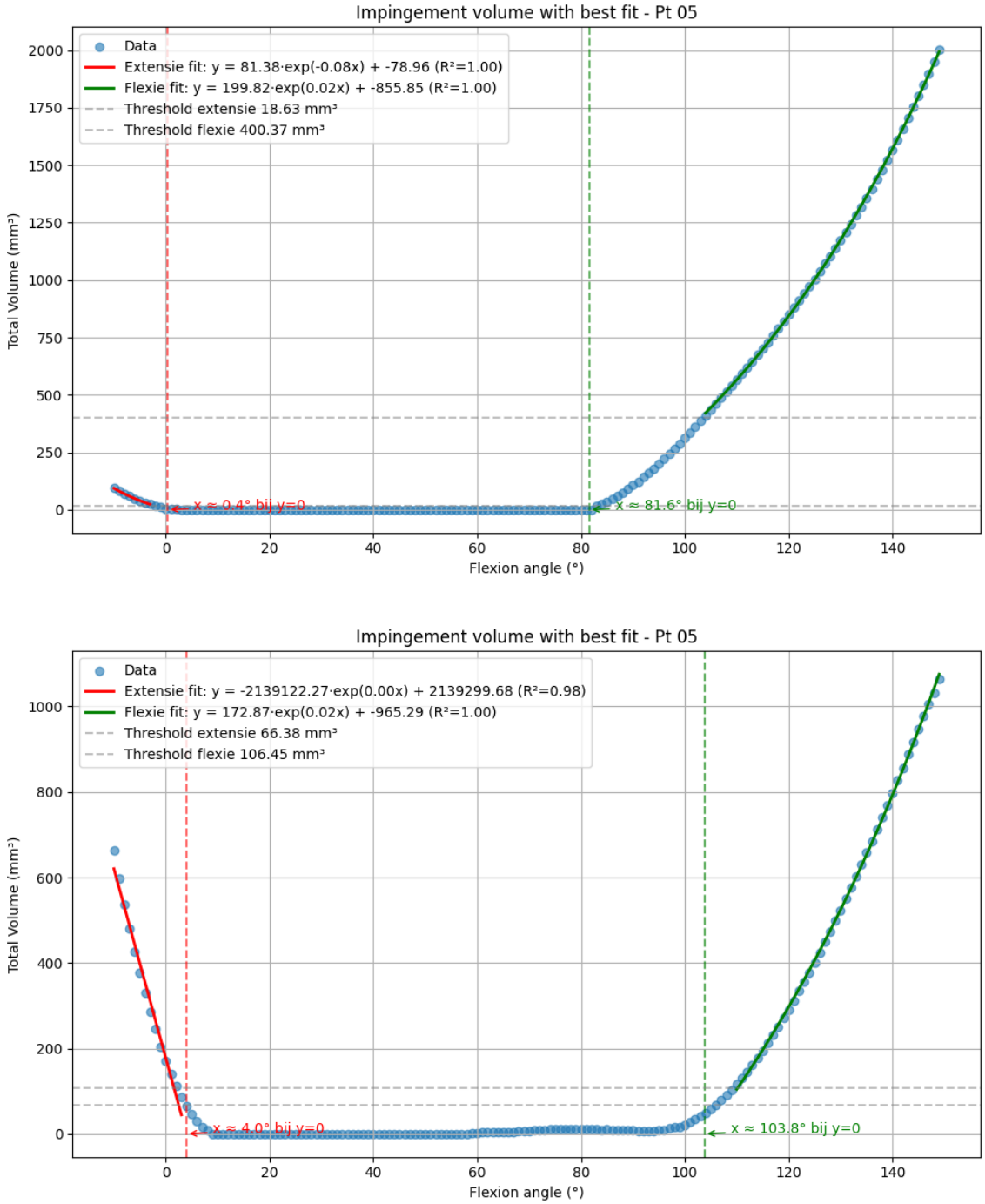

Figure F5: *Detected impingement volume (blue points) versus the flexion angle for the radiohumeral region (top) and ulnohumeral region (bottom) of patient 5. The exponential fits identify the onset of impingement (vertical dashed line).*

Patient 6

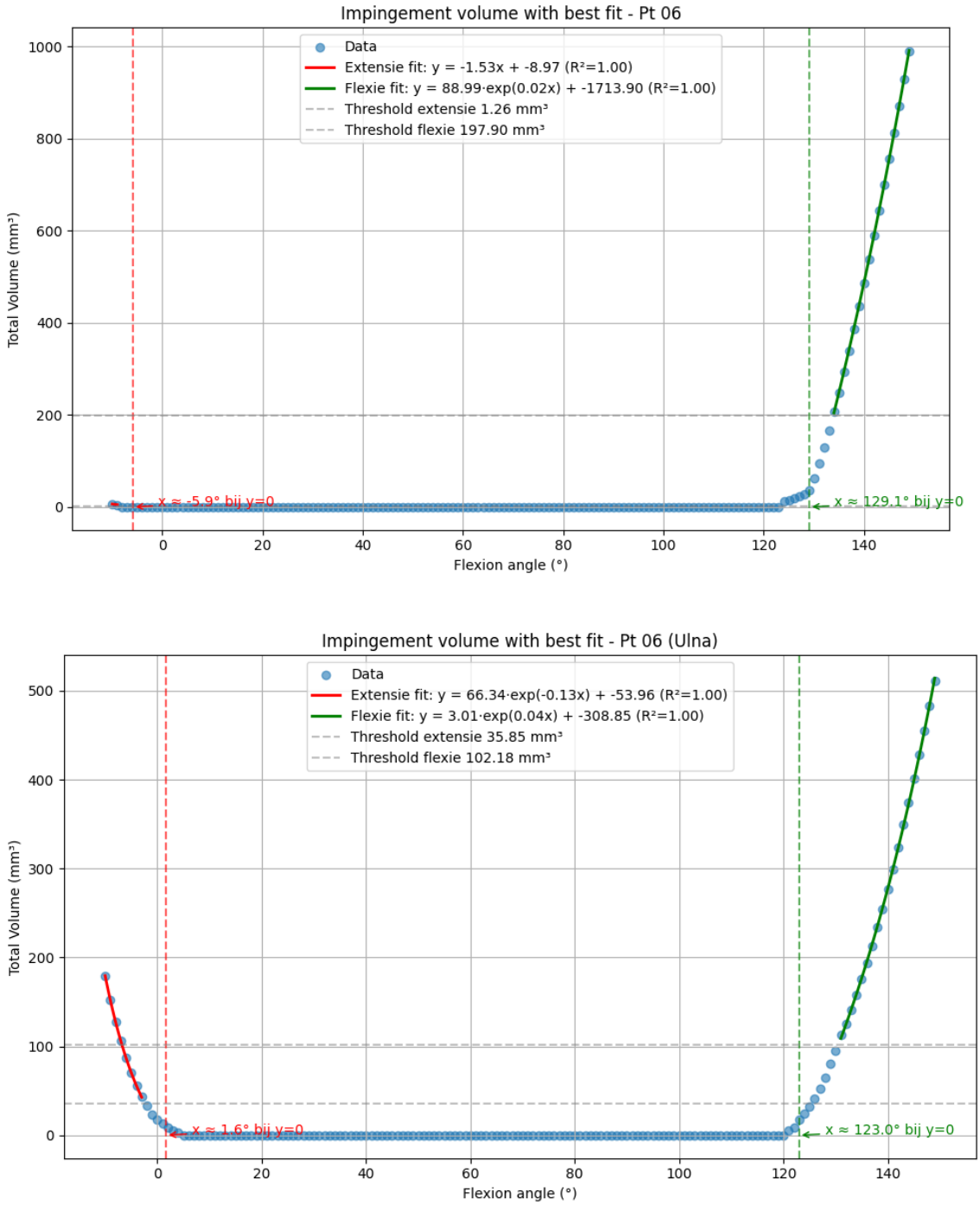

Figure F6: *Detected impingement volume (blue points) versus the flexion angle for the radiohumeral region (top) and ulnohumeral region (bottom) of patient 6. The exponential fits identify the onset of impingement (vertical dashed line).*

Patient 7

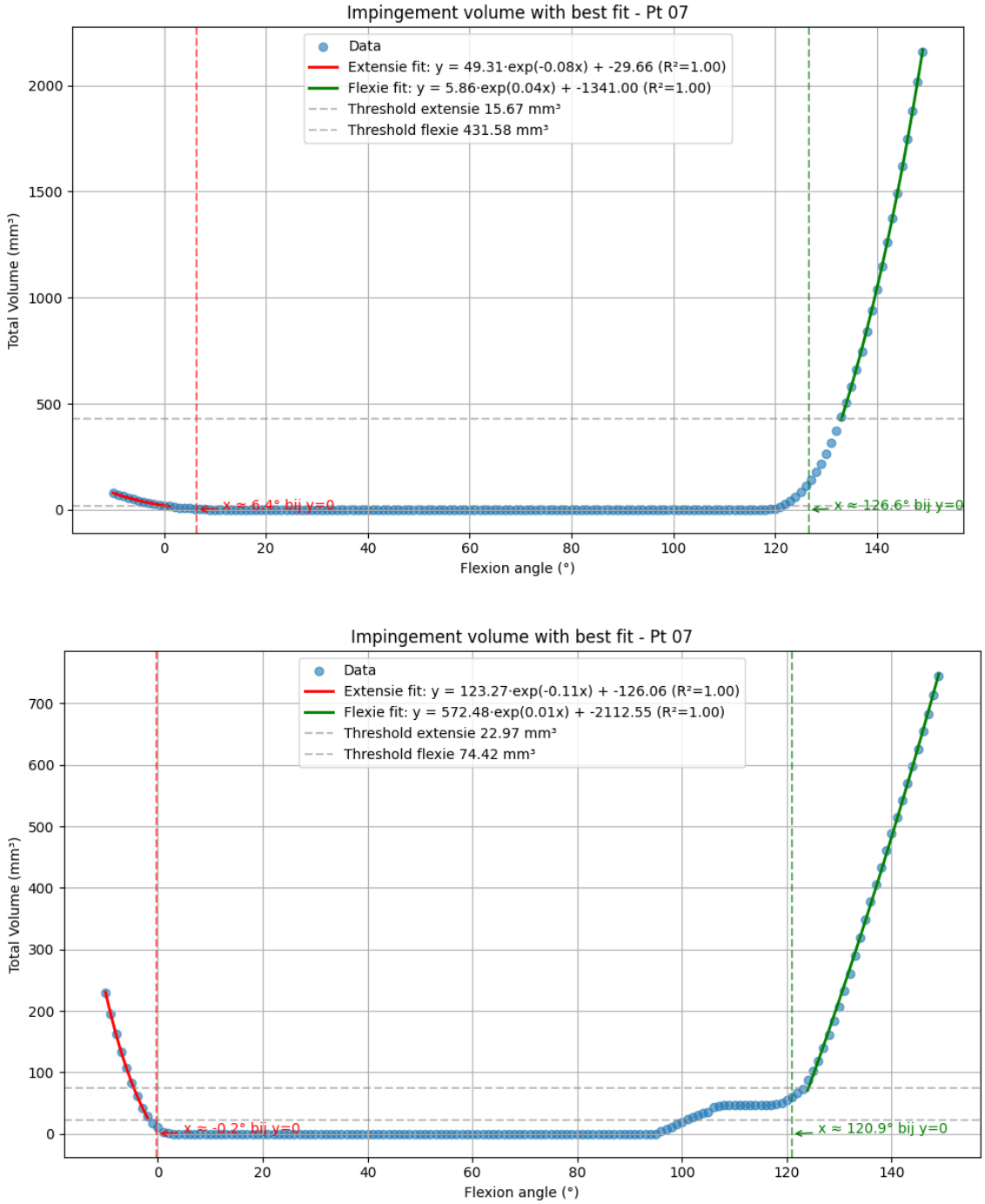

Figure F7: *Detected impingement volume (blue points) versus the flexion angle for the radiohumeral region (top) and ulnohumeral region (bottom) of patient 7. The exponential fits identify the onset of impingement (vertical dashed line).*

Patient 8

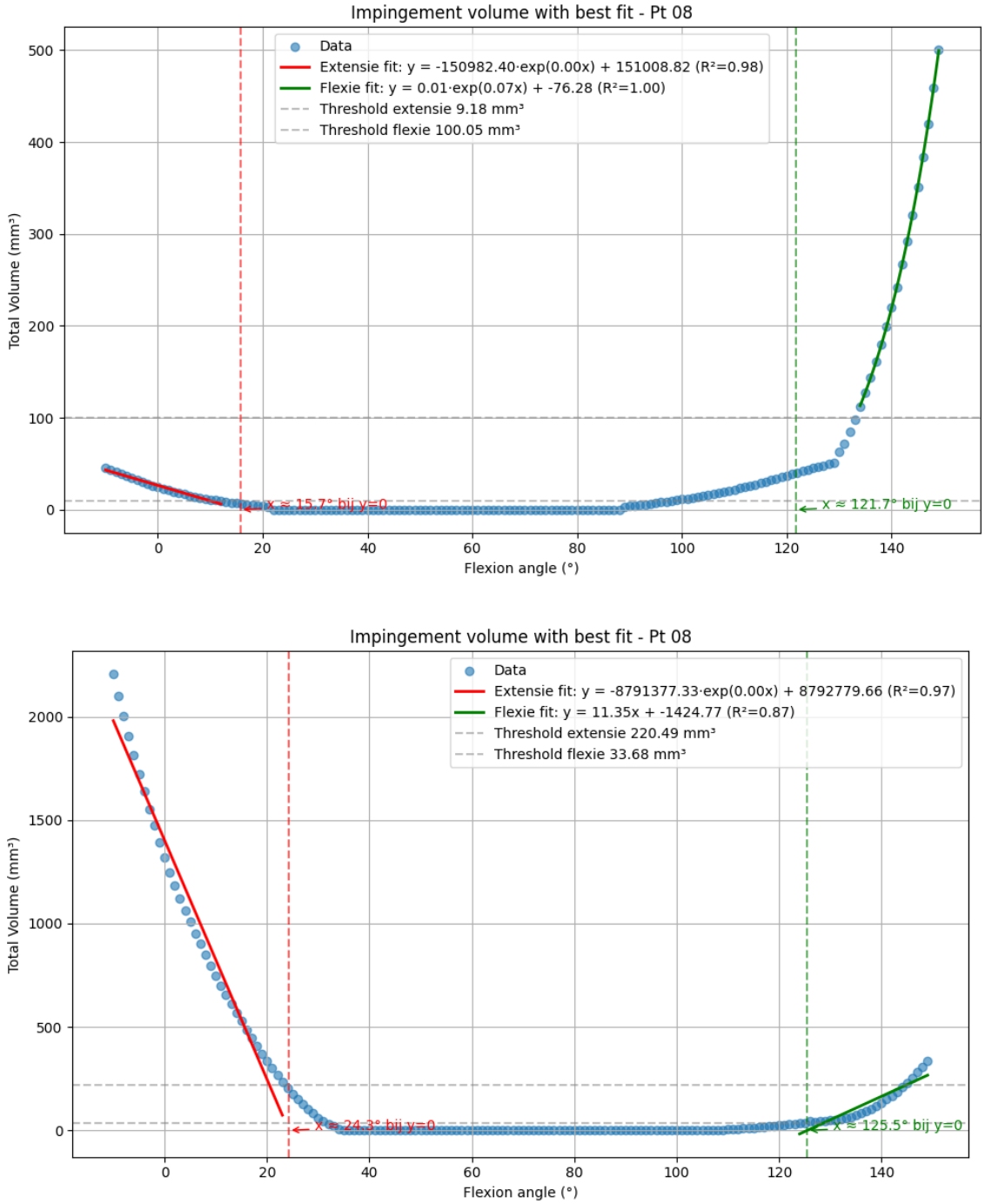

Figure F8: *Detected impingement volume (blue points) versus the flexion angle for the radiohumeral region (top) and ulnohumeral region (bottom) of patient 8. The exponential fits identify the onset of impingement (vertical dashed line).*

Patient 9

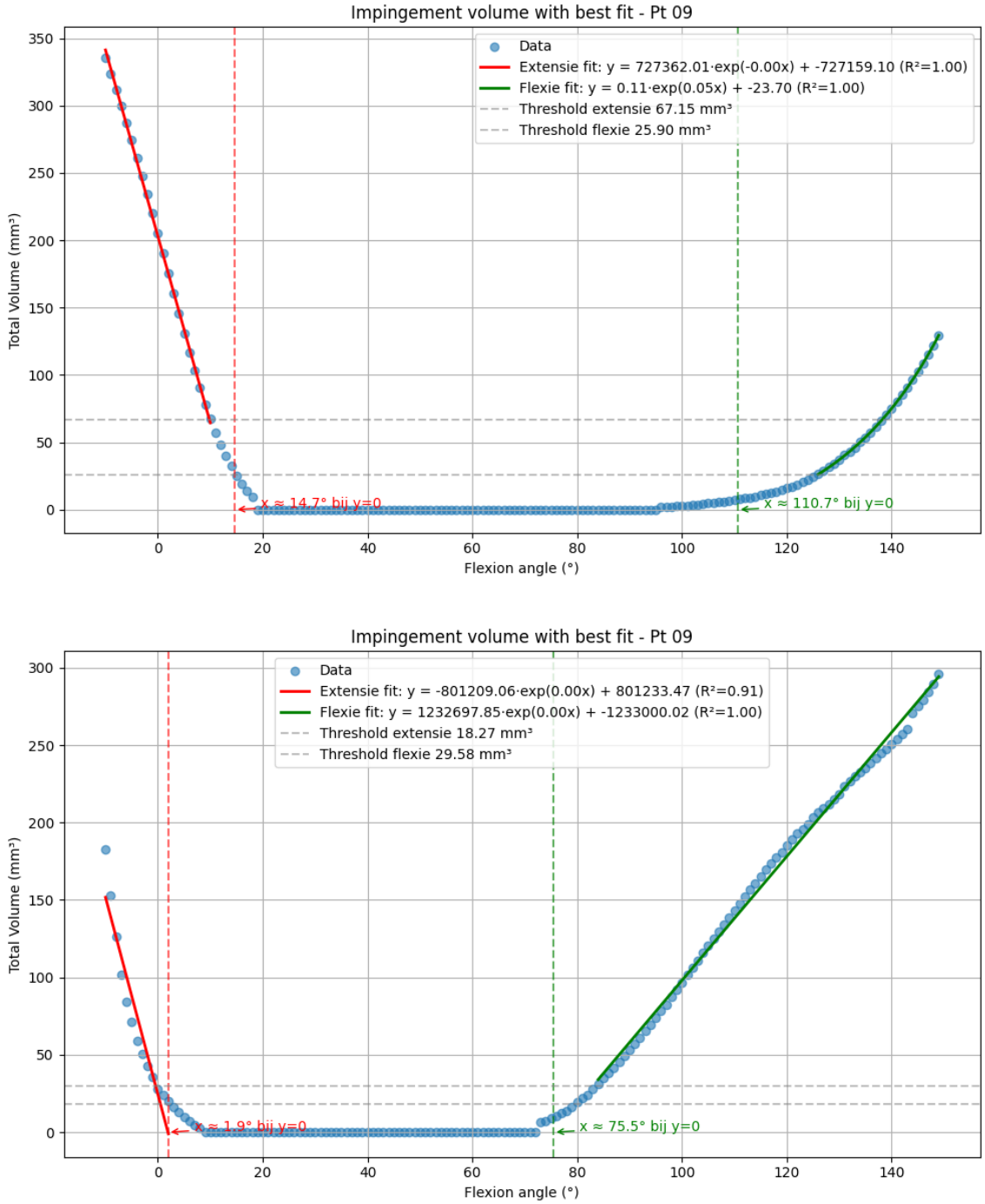

Figure F9: *Detected impingement volume (blue points) versus the flexion angle for the radiohumeral region (top) and ulnohumeral region (bottom) of patient 9. The exponential fits identify the onset of impingement (vertical dashed line).*